Universidad Zaragoza
1542

Final Master Project

Correlation of memristive behaviour with perovskite solar cell performance.

Author

Álvaro Muñoz Martín

Supervisors

Emilio J. Juarez-Perez

María Cristina Momblona Rincón

Master's in Nanostructured Materials for Nanotechnology Applications

Universidad de Zaragoza

Department of Chemical Engineering and Environment

September 2023

Facultad de Ciencias Universidad Zaragoza

CSIC Consejo Superior de Investigaciones Científicas

INMA Instituto de Nanociencia y Materiales de Aragón

Acknowledgments

First of all, I would like to thank my supervisors Emilio J. Juarez-Perez, Cristina Momblona and María Bernechea for his dedication and commitment to this project, as well as his invaluable help at all times in resolving my doubts and describing how a job of this calibre should be carried out. They carry out both the research and the tutoring with great enthusiasm. I would also like to thank Álvaro Larrotiz for being my project partner with great comradeship. Financial support from EASI Project (Perovskite-nanocrystal heterojunction solar cells with extended absorption and improved performance. Ref: PID2019-107893RB-I00. Funded by Agencia Estatal de Investigación) is gratefully acknowledged.

I also would like to thank to Enrique Carretero and Carmen Cosculluela of the Department of Applied Physics for their collaboration allowing me to have access to the Thermal Evaporator for the deposition of Au, Nuria Navascués for performing the XRD measurements, Luis Angurel for laser's etching of FTOs and Ana Isabel Gracia Lostao for allowing me to use the UV ozone cleaner from her research group.

On a personal level, I thank Carlota for putting up with me and supporting me throughout this year. Also to my parents, without them this would have been impossible.

ABSTRACT

In this Final Master Project, the working premise is the development and characterization of high efficiency and stable methylammonium lead iodide (MAPI)-based perovskite solar cells (PSCs), as well as the study of their memristive behavior. Throughout the project, the method of formation of perovskite thin film and, subsequently, of the formation of the photovoltaic cells in humidity-controlled conditions has been optimized. The focus of the project is the preparation of different perovskite solar cell structures by changing their ETLs, namely, 1)c-SnO_2, 2)c-SnO_2/m-TiO_2, 3)c-TiO_2 and 4)c-TiO_2/m-TiO_2 has been used. Then, the efficiency and stability of PSCs will be studied with a 'Solar Cell I-V Test System' under both dark and sun illumination conditions by means of an artificial solar illuminator. The memristive behaviour of these same PSCs will also be studied by means of cyclic voltammetries with a potentiostat/galvanostat under both dark and sun illumination. Finally, the results obtained will be used to correlate the solar efficiency with the memristive behaviour of all the PSCs structures studied. On the other hand, the crystallographic and morphological properties of the layers in the photovoltaic cell will be characterized by means of a structural characterization technique.

RESUMEN

En este Proyecto Fin de Máster, la premisa de trabajo es el desarrollo y caracterización de células solares de perovskita (PSC) de alta eficiencia y estables basadas en la perovskita yoduro de plomo de metilamonio (MAPI), así como el estudio de su comportamiento memristivo. A lo largo del proyecto se optimizará el método de formación de la capa delgada de perovskita y, posteriormente, de la formación de las células fotovoltaicas en condiciones controladas de humedad. El proyecto se centra en la preparación de diferentes estructuras de células solares de perovskita cambiando sus ETLs donde se han utilizado 1)c-SnO_2, 2)c-SnO_2/m-TiO_2, 3)c-TiO_2 y 4)c-TiO_2/m-TiO_2. A continuación, se estudiará la eficiencia y estabilidad de las PSCs con un "Sistema de Ensayo I-V de Células Solares" tanto en condiciones de oscuridad como de iluminación solar mediante una fuente solar artificial. También se estudiará el comportamiento memristivo de estas mismas PSCs mediante voltametrías cíclicas con un potenciostato/galvanostato tanto bajo iluminación solar como en condiciones de oscuridad. Finalmente, los resultados obtenidos se utilizarán para correlacionar la eficiencia solar con el comportamiento memristivo de todas las estructuras de PSCs estudiadas. Por otro lado, se caracterizarán las propiedades cristalográficas y morfológicas de las capas de la célula fotovoltaica mediante una técnica de caracterización estructural.

INDEX

1. INTRODUCTION

1.1 BACKGROUND

The great socioeconomic development of the last decades has led to the emergence of two structural problems: Energy scarcity and environmental pollution. In view of this, photovoltaic (PV) technology is emerging as the energy source of the future, as a clean and renewable energy technology capable of converting sunlight directly into electrical energy.[1] The 1970s marked the development and commercialization of the hegemonic PV technology until recently: Si-solar Cell. The 21st century brought the emergence of new materials potentially applicable in this technology, being the field of 'organic–inorganic hybrid perovskite solar cells (PSCs)' the fastest-growing photovoltaic in last few years. This light-harvester material has a general formula ABX_3, where A is a monovalent organic cation (such as $CH_3NH_3^+$ or MA^+; $CH_3(NH_2)_2^+$ or FA^+), B is a divalent metal cation (such as Pb^{2+}, Sn^{2+}, Ge^{2+}), and X is a monovalent halogen anion (I^-, Br^-, Cl^-). What makes them the 'photovoltaic material of the future' is their strong absorption in the visible region,[2] exciting optical properties (long carrier diffusion length up to ~1 μm,[3] weak exciton binding energy values ~45 meV,[4] high carrier mobility close to 25 $cm^2\ V^{-1}s^{-1}$,[5] and low charge recombination rate on microseconds time scale), their outstanding optical tunability (strong absorption in the visible region) and low-temperature solution processability (low-cost fabrication techniques).[2] Its bandgap can be easily tuned by adjusting its A, B, X composition and structure.

In 2022, according to the National Renewable Energy Laboratory (NREL) of the US, perovskite solar cells reached a power conversion efficiency (PCE) record of 26.1%, up to the level of the commercial silicon cell even overpassing the multicrystalline Si solar cell record efficiency (23.3%).[6] Nevertheless, stability of PSCs (loss of efficiency with time) is still lower than commercial ones, which is placing a great deal of effort on the scientific community to understand how to improve stability and understanding the reasons behind its degradation.[7,8]

The phenomenon responsible for the functioning of a solar cell is the photovoltaic effect, basically, exposure of a semiconductor, like perovskite, to an energy of a specific wavelength results in the emission of an electron and the creation of two energy regions in the boundaries of the semiconductor (P-type is the electron-defective region (+ charge) and N-type the region with an excess of electrons (- charge)).[9] The union of these zones forms what is known as the '*p-n* junction' where the electric current is produced with the photon interaction. Solar radiation presents a wide spectrum of photons with different energies (see Figure 1). On the other side, a semiconductor material exhibits a bandgap, which is the minimum energy that must be absorbed by a material's electron to produce the

photoelectric effect (or energy band hopping). Only solar radiation photons with energy above the bandgap will achieve the above-mentioned effect with the consequent formation of electron-hole pairs, responsible for the electric current. As a result, when the incident photon energy exceeds this band gap, a steady electrostatic field is created, and the resulting voltage difference causes electrons to flow from the junction's n-side to its p-side. The higher the optical absorption capacity of the semiconductor material, the higher the photoelectric efficiency of the solar cell. It is also beneficial for the creation of electric current that there are materials in boundaries with the capacity to extract charges to transport them from the *n-p* junction to the external circuit.[10]

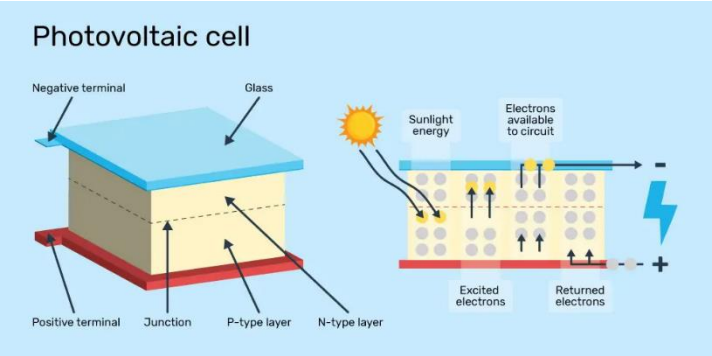

Figure 1.: Scheme of a photovoltaic cell.[11]

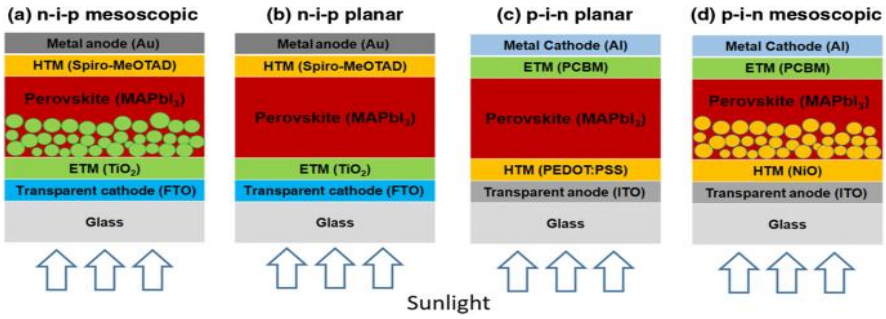

Figure 2.: layered structure four typical of perovskite solar cells (a) n-i-p mesoscopic, (b) n-i-p planar, (c) p-i-n planar, and (d) p-i-n mesoscopic[15]

In view of this, the typical PSC structure will be the light-harvester (perovskite) layer embedded between two charge transport layers, electron transport layer (ETL) and hole transport layer (HTL). The different PSCs structures are mainly four depending on the first layer passing the sunlight (see Figure 2). They can be classified as regular (n-i-p) and inverted (p-i-n) structures depending on which transport (electron/hole) material is present on the exterior portion of the cell/encountered by incident light first. These two structures can be further divided into two categories: mesoscopic and planar structures.[12] As of 2018, the best mesoscopic n-i-p device has exhibited a PCE 21.6%,[13] whereas the highest reported efficiency of a planar n-i-p cell 20.7%,[14] nevertheless, mesoscopic device has manufacturing disadvantages: it requires a thinner thickness (less than 300 nm) and cannot be manufactured by a low-temperature process unlike the planar structure.[12]

The three major operations of the photovoltaic system are: (1) absorption of photons followed by free charge generation (2) charge transfer and (3) charge extraction. A PSC is exposed to sunlight, which causes the perovskite to absorb light, make excitons, and produce charge carriers (electron

and hole) because of exciton dissociation (perovskite's weak exciton binding energy is the key parameter). At the boundary between the charge-transporting layer and the perovskite layer, exciton dissociation takes place. The anode, which is typically transparent conductive oxide glass, receives the electron once it is detached from the hole and introduced into the electron-transporting layer (ETL). The hole is simultaneously injected into the hole-transporting layer and then moves to the cathode, which is typically made of metal. Working and counter electrodes, respectively, gather the electrons and holes, which are then delivered to the external circuit to create current.[12]

1.2 MATERIALS OF PEROVSKITE SOLAR CELL

In the previous section we mentioned what the configuration of a perovskite solar cell should be, and we will now discuss what type of materials should be used in each layer. Depending on the type of solar cell being used, different materials are used to create the various layers. It should be noted that the materials discussed in this section are those used in this project. The structure used in this project is of the type 'n-i-p' following the nomenclature 'glass/transparent conductive oxide *'(TCO)/ETL/perovskite/HTL/metal electrode'* (see Figure A1[16]).

The proper functioning of a PSCs requires the use of **'Transparent conductive oxide' (TCO)** layers, which collect charge carriers from ETL and transfer them to the external electric circuit. They are one of the most important components of a solar cell because low charge collecting efficiency of a TCO layer may deteriorate the cell performance.[17] Another important aspect to guarantee is its transparency since it is the layer through which solar radiation impacts, it should not affect it optically so that the photovoltaic process in the light absorber layer is maximized. One of the most used TCOs in photovoltaic technology is '**Indium Tin Oxide (ITO)**' glass substrate, in which a 100nm layer of ITO is deposited on a transparent glass. It is highly valued as TCO because of its good electrical conductivity at room temperature, originated from free carriers in Sn^{4+}/In^{3+} sites and vacancies in regular oxygen lattice, and its high transparency in the visible range.[17] Its main drawback lies in the partially destruction of its charge collection properties when an annealing process (processing of other layers) ($T > 250ºC$) is applied on it.[18] As certain device layouts in the project require these annealing processes, we opted to choose another TCO that can be used in all of them:

- **Fluorine-doped Tin Oxide (FTO)** substrates: a layer of 600-800 nm of FTO is deposited on a transparent glass. It also presents a characteristic transparency in addition to having a higher tolerance to annealing processes, supposing a great advantage with respect to ITO films. A high surface roughness characterizes FTO films so compaction with ETL layer must be taken with caution, ensuring that the interface does not suppose a problem for electron extraction efficiency.[19]

Several studies are being conducted on how to improve the performance of **ETL** layers with the premise of improving the efficiency of PSCs. For efficient PSCs, the **ETL** should meet the following criteria: a) good energy-level alignment for efficient electron extraction and hole blocking, b) high electron mobility to guarantee fast electron transport within the ETL, c) high transmittance to reduce the optical energy loss, d) high stability, and e) easy processing and low cost.[20,21] To properly form inorganic materials as ETL-films, aggressive annealing processes are required, most of them exceed 150 degrees and are therefore incompatible with a low-cost manufacturing process or application on flexible substrates.[22] For instance, Organic conducting materials can be solution-processed easily but their environmental, thermal, and photostability is a great concern. Many other low-temperature processed semiconductor metal oxides such as zinc oxide (ZnO) or metal sulfide (CdS) show many disadvantages: 1) poor thermal stability which hinders effective perovskite annealing, 2) a historically lower device efficiency,[23,24] 3) Cd can diffuse into the perovskite and react with $MAPbI_3$ forming an electrical barrier with an overall reduction in performance.[25]

In the project three types of **ETL-films** have been analyzed: **Tin Oxide-SnO_2, Compact-TiO_2 and mesoporous-TiO_2**, the latter two have historically been used as ETL for photovoltaic cells (suitable band alignment, excellent optoelectronic property with bandgap 3.2-3.4 eV and stability)[26,27] but also they present many drawbacks, for instance, surface desorption of molecular oxygen which affects the device perfomance.[28] SnO_2 shows a series of physicochemical characteristics that convert it into a more ETL-promising material than TiO_2: 1) A wide bandgap (E_g = 3.6-4.0 eV) and high transmittance over the whole visible spectra. 2) It has a bulk electron mobility (~100-200 $cm^2V^{-1}s^{-1}$) much higher than anatase TiO_2 (~0.1-1 $cm^2V^{-1}s^{-1}$) or mesoporous TiO_2 (~0.01 $cm^2V^{-1}s^{-1}$) improving a lot the electron transport efficiency and reducing the recombination loss[20] 3) It owns deep conduction band with an excellent band energy at ETL/perovskite interface (band edge E_g, of about 0.3 eV lower than that of anatase TiO_2) enhancing the electron extraction and hole blocking (see Figure 3). Also noteworthy is its low-temperature processing/fabrication (T <200 °C), compatible with flexible solar cell and large-scale commercialization.[21,23]

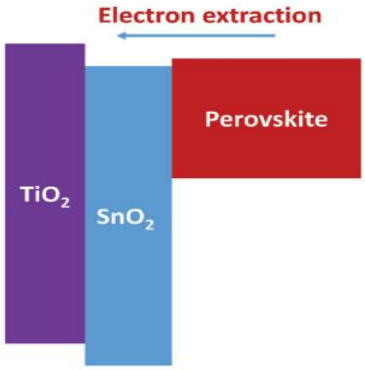

Figure 3.: Left) Band alignment of SnO_2, TiO_2, and perovskite layer. SnO_2 has a deeper conduction band than TiO_2 and many other ETL. SnO_2 can form good band alignment with perovskite layer, better electron extraction.[28]

As already mentioned, the light-harvester of a PSCs device is a **'metal halide perovskite'**. In this project we have used methylammonium lead iodide or MAPI ($CH_3NH_3PbI_3$) (see Figure 4), mainly due to its exceptional optoelectronic properties, which are responsible for the higher power

conversion efficiencies (25.8 % is the record PCE value obtained to date for a single junction PSC, thanks to Researchers at South Korea's UNIST):[29] a high absorption coefficient in visible region[30] and an appropriate bandgap (Eg = 1.6 eV),[31] long carrier diffusion length (14.0 ± 5.1 μm)[32] and high carrier mobility (10 cm^2 V^{-1} s^{-1})[33].

The other aspect that sets PSCs ahead of other PV technologies lies in MAPI processing and perovskite materials in general from a wide variety of deposition techniques, from solution- to vacuum- deposition.[34] Due to its simple dissolution in polar aprotic solvents, like DMF or DMSO, thin-film processing techniques, like spin coating (small scale PSCs manufacture) or inkjet printing (large scale PSCs manufacture), can be carried out at low cost.[35] The easy fabrication of thin-film perovskites makes it valuable for its incorporation into various device architectures, such as planar, mesoporous, single solar cells or tandem devices (junction of 2 or more single solar cells) expanding the possibilities for future applications. Last but not least, $CH_3NH_3PbI_3$ can be processed at relatively low temperatures (up to 100°C), reducing the thermal stress on the device and enabling compatibility with flexible and low-cost substrates.[36,37]

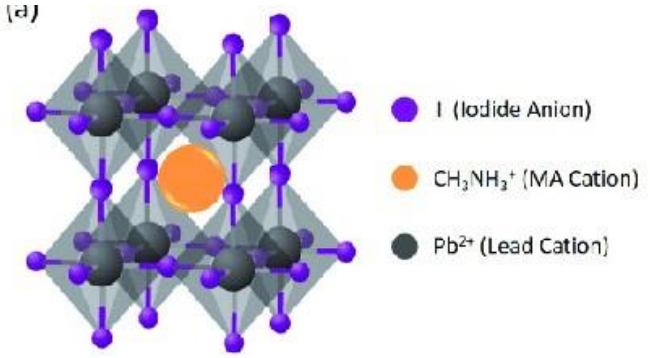

Figure 4.: Structure of MAPI.[20]

The last two layers of a PSCs device are the **HTL** and the **metal electrode**. Hole transport layers **(HTLs)** in PSCs are critical to device functionality and represent a major bottleneck to further enhancing device stability and Power Conversion Efficiency (PCE). In all the devices manufactured in the project, Spiro-OMeTAD has been used as a solid-state **HTL**, which has gained enduring popularity for its ease of processing (film-forming properties) and somewhat favorable HOMO-VB match with MAPI perovskite (LUMO of spiro-OMeTAD is positioned more than 2 eV above the conduction band (CB) of MAPI, which indicates good electron blocking abilities).[39] Due to its amorphous nature, it has been calculated that hole mobility in pristine spiro-OMeTAD to be 2 × 10^{-4} cm^2 V^{-1} s^{-1}, smaller than that of perovskites by multiple orders of magnitude,[22] which means that it limits charge transit times. To solve it Spiro-OMeTAD is p-doped, e.g. CoTFSI, LiTFSI or tBP, to increase the concentration of majority charge carriers and improve conductivity. Although LiTFSI is necessary to improve the hole conductivity, Li^+ ions easily migrate toward the film surface, which, given the highly hydrophilic nature of LiTFSI, results in a higher infiltration of oxygen and moisture and thus accelerated degradation.[40] tBP increases the LiTFSI solubility and reduces phase segregation ensuring a better film quality but its corrosive nature harms the perovskite material. These drawbacks are only partially palliated by the formation of the Li^+-tBP complex, while

similar degradation effects can be observed by doping the HTM via chemical oxidization of CoTFSI and tBP.[41,42]

As an **electrode**, excellent conductivity and suitable work function are prerequisites to extract, collect and transfer charge carriers efficiently. Currently, the benchmark state-of-the-art PSCs are usually noble-metal, such as gold, which is the material used in our project, which have a low sheet resistance R_{sq} (less than 1 Ω sq^{-1}) and high light reflectivity.[43] Figure 5 shows the 4 working device layouts in the project.

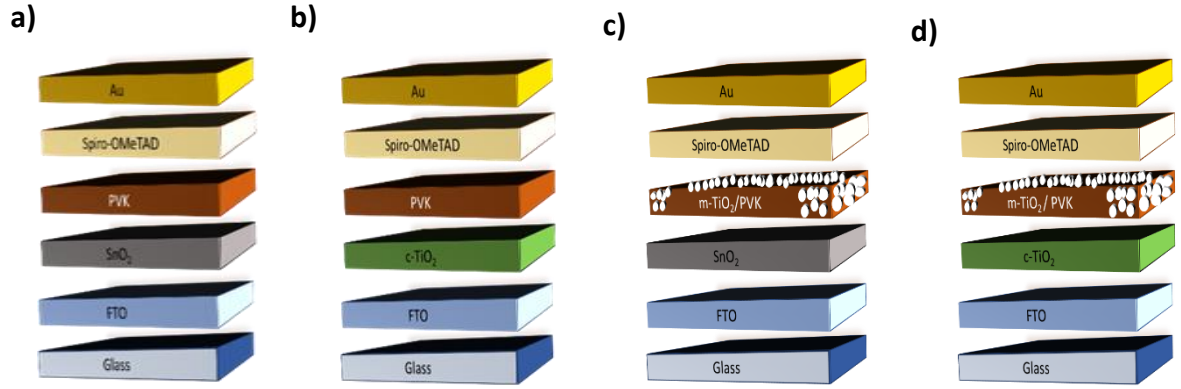

Figure 5.: Types of PSCs structures used in the project: a) FTO/SnO_2/MAPI/Spiro-OMeTAD/Au; b) FTO/TiO_2/MAPI/Spiro-OMeTAD/Au, c) FTO/SnO_2/m-TiO_2/MAPI/Spiro-OMeTAD/Au and d) FTO/c-TiO_2/m-TiO_2/MAPI/Spiro-OMeTAD/Au

1.3. CHARACTERIZATION OF A SOLAR CELL

The most widespread method for the study of a solar cell device is through the study of Current density (J)-voltage (V) curves under simulated 1 sun illumination (100 $mWcm^{-2}$), whose interpretation provides us with the 'figures of merit' of an ideal solar cell.

When a solar cell is not subjected to illumination (natural or artificial), it works in 'Dark conditions' and its diode behavior can be analyzed by a J-V measurement (Figure 6.Left)):

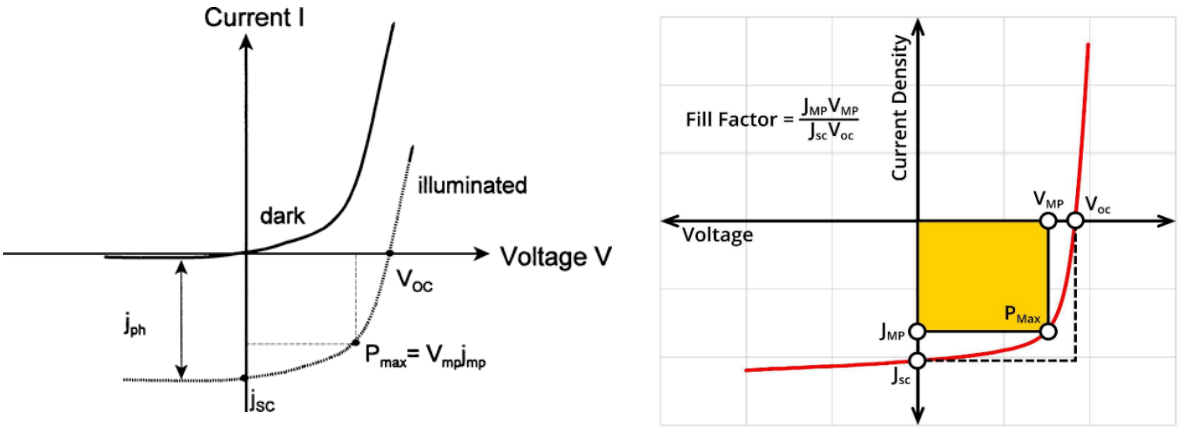

Figure 6.: Left) J-V curve of a solar cell. Dark (line) and illuminated (dotted line) conditions.[44] Right) Characteristic solar cell curve with its PV parameters.[45]

Figure 6.Left) shows how the application of illumination (Sun conditions) on the solar cell shifts the diode shape curve to a lower position on the graph due to the photocurrent generation. The figures of merit of a solar cell operating under light can be extracted from the corresponding J-V curve (see Figure 6.Right)).

- Open-circuit voltage (V_{oc}) (unit: volts): the maximum voltage available from a solar cell which occurs at zero current. The V_{oc} corresponds to the amount of forward bias on the solar cell due to the bias of the solar cell junction with the light-generated current. It is higher for materials with a larger band gap and for ideal solar cells, it would be independent of the illumination intensity.[45]
- Short-circuit current density (J_{sc}) (unit: mA/cm^2): maximum current through the solar cell when the voltage across it is zero (when solar cell is short circuited). It is due to the generation and collection of light-generated carriers, consequently, the larger band gap of a material, the smaller J_{sc}.[45]
- Shunt resistance (R_{SH}) (units: Ohms): It is typically due to manufacturing defects. Low shunt resistance causes power losses in solar cells by providing an alternate current path for the light-generated current. Such a diversion reduces the amount of current flowing through the solar cell junction and reduces the voltage from the solar cell. It should be as high as possible.[45]
- Series resistance (R_s) (units: Ohms): Due to movements of current through the emitter and base of the solar cell and contacts between metal connections and the solar cell. It should be as low as possible.[45]
- J_{MP} (units: Ohms): Current density at maximum power point.[45]
- V_{MP} (units: volts): Voltage at maximum power point.[45]
- P_{max} (units: watts or Js^{-1}): The maximum output power (also known as maximum power point).[45]
- Hysteresis index (HI) (adimensional): It measures the difference in magnitude and type of J-V curve of the Forward Scan Direction (FWD) versus the Reverse Scan Direction (RSD).

$$\boldsymbol{HI = \frac{PCE(RVD) - PCE\ (FWD)}{PCE\ (RVD)}}$$

- Fill factor (FF) (adimensional): ratio of the actual power of the cell to what its power would be if there were no series resistance and infinite shunt resistance. It is related to the shape of the J-V curve and ideally as close as possible to 1.

$$FF = \frac{J_{MP}V_{MP}}{J_{SC}V_{OC}}$$

- Power Conversion Efficiency (PCE) (adimensional or %): It represents the fraction of incident sunlight converted into electricity. It is therefore the key parameter that determines the suitability of a solar cell and allows a comparison between them. It can be calculated with the ratio between the device power and the incident light power.

$$PCE = \frac{J_{SC}V_{OC}FF}{Light\ power\ (\frac{W}{cm^2})}$$

1.4 MEMRISTIVE BEHAVIOUR

Memristivity refers to the property of a memristor, which is a type of passive two-terminal electronic component. Professor Leon Chua noted that, in addition to resistors, capacitors and inductors, a 4th component was missing to complete the 'four fundamental two-terminal circuit elements' (see Figure 7.A)):a component that related charge (Q) to magnetic flux (Φ), the above-mentioned **memristor** (contraction for memory resistor): a device with the ability to "remember" the amount of charge that has flowed through it in the past, and to adjust its resistance accordingly.[46,47] Memristors have many potential applications, including in memory storage and neural networks. The properties of minimum power consumption, simple composition and compatible processing make memristors a great potential candidate for superior characteristics in many applications, such as novel logical devices and artificial neuromorphic systems.[48]

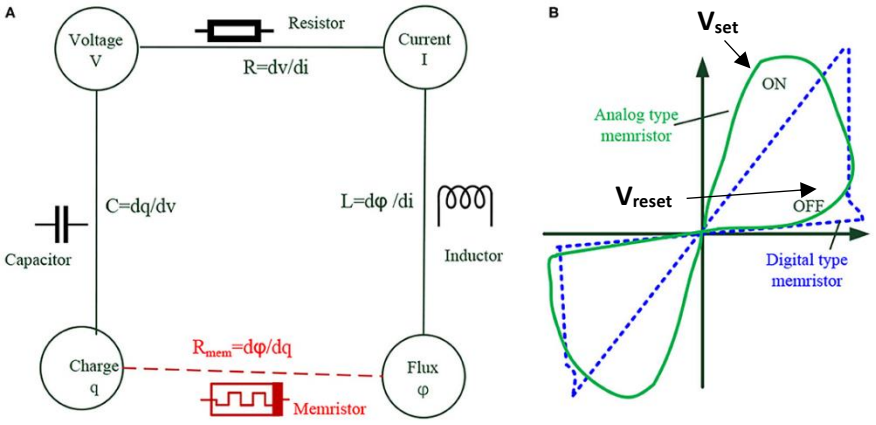

Figure 7.: A) Basic theoretical circuit elements, B) Hysteresis I–V loop of memristor.[47]

The cause of the memristive behaviour of perovskite-MAPI has been explained by several mechanisms, but the most common one is the **'ionic migration'**: motion and accumulation of ions inducing a doping effect.[53] The positively charged ions or vacancies moved to the Au side during positive poling and accumulated there, leading to n-doping in perovskite on the Au side. Similarly,

the remaining negative spacecharge layer can p-dope the perovskite layer close to HTL, forming a p–i–n homojunction structure. A reverse bias can flip the p–i–n structure to n–i–p by forcing ions or ion vacancies to driftin the opposite direction. The memristive dark- and photocurrenthysteresis can also be explained well by the time-dependent drift of ions under the field. This ion movement can result in changes in device performance and can be considered a form of "memory" as it alters the device's resistance or conductivity.[54]

Typically, a memristor makes a transition from a high to a low resistance state (HRS−LRS) when a certain threshold forward voltage is passed, which can be restored to the initial state by a reverse voltage sweep.[47] There are two important voltages: the set voltage and the readout voltage. The set voltage is the voltage applied to the memristor to establish a specific resistance state or "set" state. It determines the resistance value of the memristor and sets it to a desired level. On the other hand, the readout or asking voltage is the voltage applied to the memristor to read or interrogate its resistance state. This voltage is used to measure the resistance of the memristor and obtain information about its stored state. These voltages play crucial roles in the operation and functionality of memristors. This property allows memristors to act as a type of non-volatile memory, which means that they can retain information even when the power is turned off.[48]

The memristive capacity of a PSCs can be evaluated by studying its performance parameters:

- ON/OFF current: ratio of the current measured in the high resistance state (HRS) to the current measured in the low resistance state (LRS). The higher the ratio means that the hysteresis in the loop will also be higher and therefore the memristive behavior will be more noticeable.[48]

$$\frac{ON}{OFF} = \frac{R_{HRS}}{R_{LRS}} = \frac{I_{LRS}}{R_{HRS}}$$

- V_{set} or V_{reset} (Units: Volts): Voltages at which there is an abrupt change in the slope of the J-V curve. Normally, V_{set} is positive and V_{reset} negative. They are associated with changes in the dynamics of charge carriers.[48] In figure 7.B) V_{set} and V_{reset} are indicated.
- Endurance time (Resistant or not to a number of Cycles): In cyclic voltammetry, successive cycles are performed to check how they affect the nature of the I-V loop. This time determines until which cycle the memristive behavior remains intact.[47]
- Shape of voltammetric curve: When performing cyclic voltammetry, the sample curve can take on two predominant forms: (1) Bottle-shaped curve (FigureA2.Left)), (2) Crossed Loop curve (FigureA2.Right)).

2. OBJECTIVES

2.1 GENERAL OBJECTIVE

The general aim of this project is the development of perovskite-based (MAPI) photovoltaic cells (PSCs) to study their solar cell parameters on the one hand and their memristive behaviour on the other in an attempt to correlate both phenomena. In addition, different types of PSC structures are prepared in order to observe variations in photovoltaic parameters, memristive behaviour and possible correlation depending on them.

2.2 SPECIFIC OBJECTIVES

The general objective branches into several specific objectives:

- Develop manufacturing methods for the different PSC structures based on 'thin-film formation'. Specifically, the different films that form the structures have their fabrication and deposition route, so concentrations/type of precursors, annealing temperatures and deposition techniques are varied along the experiments.
- To measure the achieved photovoltaic performance of each PSC to compare devices within the same structure and between structures.
- To obtain the figures of merit (FOM) for the memristive behaviour of each PSC in order to compare devices within the same structure and between structures. Finally, to be able to correlate solar performance with the memristive behaviour of the PSCs in each structure.

2.3 ACADEMIC OBJECTIVES

The academic objectives pursued in this work are:

• To learn to choose the right tools or methodologies correctly.

• To develop the ability to adequately plan the work to be carried out.

• To learn the use and appropriateness of bibliographical sources and citations.

• To learn to present the results in an orderly, clear, and precise manner.

3. EXPERIMENTAL PROCEDURE

The following reagents are used for the formation of the different layers of a perovskite solar cell (PSC)*:tris(2-(1H-pyrazol-1-yl)-4-tert-butylpyridine)cobalt(III) tri[bis(trifluoromethane)sulfonimide]* (FK 209 Co(II) TFSI salt), *bis(trifluorometano)sulfonimida lithium* (Li-TFSI salt), *spiro-OMeTAD* (99%), *4-tert-Butylpyridine* (98%)), *chlorobenzene anhydrous*, *1-propanol*, *anhydrous acetonitrile*, *titanium diisopropoxide bis(acetylacetonate) 75 wt. % in isopropanol* were purchased from Sigma Aldrich Corporation (Merck). *Tin (IV) oxide* (15% in

H_2O colloidal dispersion) from Alfa Aesar, *methylammoium iodide* (MAI, 98%) from Greatcellsolar Materials, *lead iodide* (99%) from TCI Chemicals. Moreover, *N,N*-dimethylformamide (DMF) and *toluene* were purchased from VWR, *dimethyl-sulfoxide* (DMSO) from Fisher Chemicals and *absolute ethanol* (EtOH) from Panreac. All the materials were used as received. The project used FTO TEC 8 (Fluorine-doped Tin Oxide) Glass substrates (20 mm x 15 mm x 2.2 mm).

Part of the manufacturing processes of PSCs are conducted within a humidity-controlled chamber (HCC) (Figure 8.Left)). This chamber is airtight and features an antechamber that enables the insertion or removal of objects without direct communication with the outside environment. Furthermore, it is connected to a vacuum pump and a nitrogen cylinder for purging, spin coating deposition and annealing of thin-films. Moreover, we have the capability to monitor the temperature, relative humidity, and absolute humidity both inside and outside the chamber due to the presence of internal and external sensors and systems (see Figure 8.Right)).

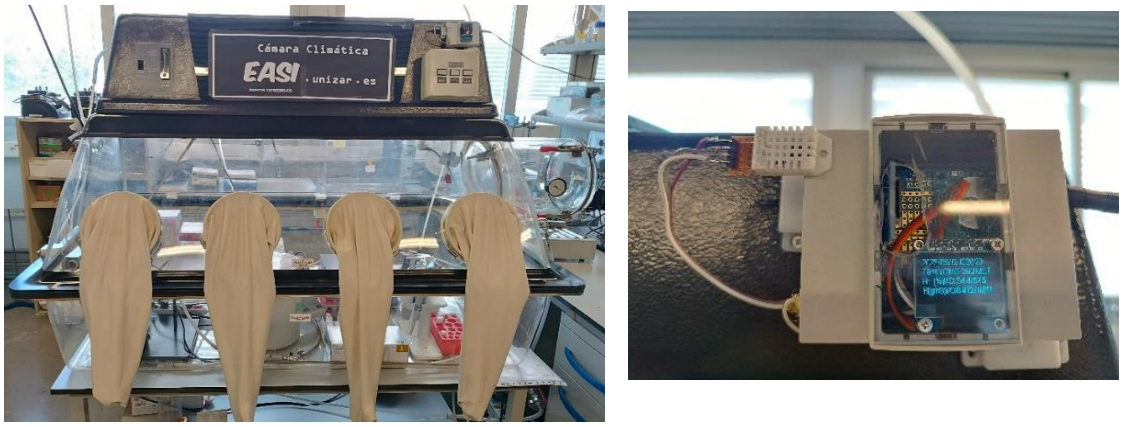

Figure 8.: Left) Photograph of the frontal view of the HCC. Right) Photograph of the device tracking absolute, relative humidity and temperature inside and outside of the HCC.

The experimental activity of the project is classified under the following headings:

- Fabrication and assembly of the different layers that form a perovskite solar cell (PSC). Optimization of thin-film perovskite formation method.
- Study of solar cell performance (photovoltaic parameters such as PCE, V_{oc}, J_{sc} and FF and hysteresis index) and stability of photovoltaic cells.
- Study of memristive behaviour (Cyclic voltammetries) of photovoltaic devices.
- Characterization of the optical, crystallographic and morphological properties of the perovskite layers by means of structural characterization techniques.

3.1 FABRICATION/ASSEMBLY OF DIFFERENT LAYERS THAT FORM A PEROVSKITE SOLAR CELL. OPTIMIZATION OF THE THIN-FILM PEROVSKITE FORMATION METHOD.

A photovoltaic device is a multilayer stack composed of different layers of different materials, each with its own function. All layers (except ETL-TiO_2 and Au) are deposited using the 'spin-coating thin-film deposition' through a spin-coater device model WS-400BZ-&NPP/LITE (Laurell Technologies) (Figure A3), operating with an extremely precise rotation control coupled with a closed, fully optimized process chamber. It allows the user to program key parameters, mainly spin speed/acceleration and spin time, to achieve uniform and controlled film thickness.

As discussed in the Introduction: The device architecture analyzed in this project are *'(TCO)/ETL/perovskite/HTL/metal electrode'* (different device layouts in Figure 4) and the corresponding experimental procedure is indicated as follows:

- Transparent conductive oxide (TCO): It constitutes the substrate PSCs. FTO substrates were etched by a laser engraving technique (Figure9.Left)), carried out by the Department of Materials and Fluids Science and Technology of Unizar (CSIC), specifically, Luis Angurel's group. Alternatively, we deployed a chemical etching method adding a few drops of 3M HCl solution on metal zinc powder onto FTO substrates producing H_2 gas reducing the tin oxide to easily removable metal tin. In chemical etching, the substrates must be covered with strips of adhesive tape both in a central strip and at the ends to prevent the reduction of tin oxide in such areas that will act as electrical contacts (Figure 9.Right)).

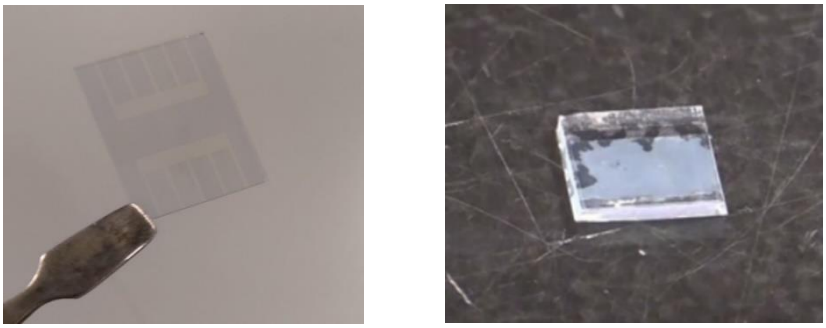

Figure 9.: Left) Laser patterned FTO substrate. Right) Chemically patterned FTO substrate.

All substrates were cleaned (after etching for FTO and as received for ITO) following these steps:

- Ultrasonication for 5 min with soapy tap water (Hellmanex solution diluted in water)
- Ultrasonication for 5 min with tap water (to remove Hellmanex)
- Ultrasonication for 5 min with deionized water
- Ultrasonication for 5 min with Acetone
- Ultrasonication for 5 min with Ethanol

Finally, the substrates were dried individually using an air gun to ensure thorough drying. Following that, immediately prior to the deposition of the ETL through spin-coating, the substrates undergo a surface treatment process involving the removal of organic residues using UV/Ozone (15 minutes on the UV Ozone Cleaner™ by Bioforce Nanosciences, see Figure A4).

- **Electron transport Layer (ETL):** We deposited two types of materials which can act as ETL, SnO_2 and TiO_2, each with a distinct thin-film deposition method:
  - ✓ **SnO_2 layer (spin coating)**: 0.53 mL of commercial reagent SnO_2 was diluted within 1,47 mL of deionized H_2O (SnO_2 aqueous colloidal solution (4 wt%)) (in air). The solution is deposited by spin-coating with the following program: 4000 rpm during 30 seconds. This allows to control uniformity and thickness, contributing to high quality film deposition with desired repeatability. To complete the SnO_2-thin film formation, substrates undergo annealing at 150 ºC for 30 minutes on a high quality hot plate (homogeneity in heat convection).
  - ✓ **Compact-TiO_2 layer (spray coating):** The working solution is 0.9 mL Sigma-Aldrich Titanium diisopropoxide bis(acetylacetonate) in 15 mL of 1-propanol (in the glovebox). The compact TiO_2 (c-TiO_2) thin-film deposition method will be different in this material with the use of 'Spray-coating', which involves the use of a spray gun or sprayer to atomize the Ti (IV) precursor dissolution into a fine mist or spray, which is then directed towards the substrates to be coated. The spray gun used in this process is 'IWATA H 5200 Hi-Line HP-TH' with 0,5 mm nozzle (Figure 10.Left)).

    The substrates are placed on a hot plate, (as shown in the figure 10.Right), at 450 ºC to emit the flow with the spray gun placed about 30 cm away with a flow of 2.3 mL/min approx. The exposure time of the substrates is around the time that the background paper turns yellow. After exposure the substrates must remain at 450 degrees for 20 minutes and then undergo a gradual cooling.

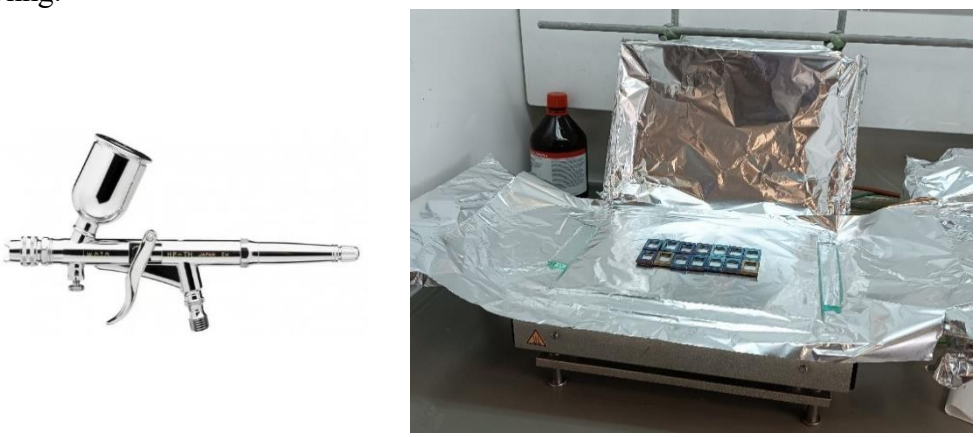

Figure 10.: Left) Spray gun model 'IWATA H 5200 Hi-Line HP-TH' 0.5 mm nozzle. Right) Substrates placed in their moulds on the hotplate at 450 ºC in a fumehood.

- **Meso-TiO_2 layer (spin-coating):** The working solution is prepared by diluting 1g TiO_2 paste (Dyesol-30NRD) in 9 mL ethanol, stirring overnight (in air). For deposition, 45 uL of the working solution is added and inmediately spin-coating is applied with the following program: 2000 rpm (acceleration 1000 rpm/s) during 15 seconds. After the deposition, the substrates must be placed on a hotplate at 70 ºC.

  To complete the m-TiO_2-thin film formation, substrates undergo a multi-step thermal treatment: **1.** 25ºC → 125 ºC in 5 mins.; **2.** 10 mins. at 125 ºC; **3.** 125ºC → 250 ºC in 5 mins.; **4.** 5 mins. at 250 ºC; **5.** 250ºC → 350 ºC in 5 mins.; **6.** 5 mins. at 350 ºC; **7.** 350ºC → 450 ºC in 5 mins.; **8.** 10 mins. at 450 ºC; **9.** 450ºC → 500 ºC in 5 mins.; **10.** 20 mins. at 500ºC; **11.** Descent to room temperature by switching off the hotplate.
- **Perovskite/MAPI (spin-coating)**: Perovskite precursor solution was prepared in an inert glovebox (<0.1 ppm O2, <0.1 ppm H_2O) using PbI_2 and MAI in the ratio of 2,9:1 (622.3 mg vs 214.6mg), then dissolved in DMF:DMSO (10:1) at a concentration of 1.49 mol/L ($CH_3NH_3PbI_3$, molar mass: 559.9 g/mol). To achieve a correct formation of the MAPI perovskite layer and to avoid pinholes or inhomogeneity layers that can cause connections between ETL and HTL, an antisolvent compound must be added to improve the crystallinity and homogeneity during the perovskite deposition process. The antisolvent chosen is toluene. The spin coating program consists of two steps: 1º) 10 secs. 2000 rpm 2º) 30 secs. 4000 rpm. 1 mL of toluene is added in the first 5 seconds of the second step. To complete the MAPI-thin film formation, substrates undergo annealing at 100 ºC for 30 mins.
- **Hole transport layer (HTL) (spin-coating):** Spiro-OMeTAD is the chosen hole transport layer. 100 mg of Spiro-OMeTAD are dissolved in 1,279 mL chlorobenzene and three dopants are added. Listing dopant solutions: 106,2 mg CoTFSI salt in 282,13 uL Acetonitrile; 213,1 mg LiTFSI salt in 411,87 uL Acetonitrile and commercial 4-*tert*-Butylpyrdine (tBP). 23 uL LiTFSI dopant solution, 18 CoTFSI dopant solution and 23 uL of tBP are added to Spiro-OMeTAD solution. On the substrate, 50 uL of Spiro-OMeTAD solution is impregnated on the substrate using a micropipette and forming a meniscus between micropipette tip and substrate. The layer was formed with a spin-coating program of 30 secs. 4000 rpm.
- **Top electrode:** The top electrode layer must exhibit metallic conductive properties. In our case, we utilize gold as the electrode material. Previous experiments performed in our group involving E-beam evaporation resulted in damage to the underlying cell layers, leading to short circuits. To overcome this issue, an alternative method was proposed, involving the thermal evaporation of gold using a metallic boat (see Figure A5. Right)). The devices using thermal evaporation presented appropriate diode/rectification behaviour. The deposition rate ranges between 10 Å/s

and 60 Å/s until an 80 nm-thick gold electrode layer is formed. Thermal evaporator (see Figure A5.Left)), owned by the Applied Physics Department of 'Universidad de Zaragoza', allows the process to be carried out at pressures around 10^{-6} mbar in a vacuum chamber. The thickness of the layer is strictly controlled with a quartz microbalance sensor (QCM) and calibrated with a Dektak XT mechanical profilometer. Prior to this project, the group determined the corresponding tooling factor for the exact thickness deposition and reading match. The metal boat (source)-substrate distance is 40 cm.

3.2 STUDY OF EFFICIENCY AND STABILITY OF PHOTOVOLTAIC CELLS.

Both the efficiency and the stability of the fabricated photovoltaic cells will be tested through the photovoltaic parameters (PCE, V_{oc}, J_{sc}, FF) obtained from the respective current density (J) *vs* Voltage (V) (J-V) curves. These measurements were carried out by using an 'Ossila Solar Cell I-V Test System' that allow the solar cells to be connected to an electrical circuit, which in turn is connected to a Source Measure Unit called UNIT-X200 (Figure 11.Right)). J-V measurements are made in dark conditions (without artificial illumination) and under artificial lighting conditions of 1 sun illumination (1000 W/m^2). Artificial lighting is produced by a LED based solar simulator (model: Oriel LHS-7320 ABA) (Figure 11. Left)).

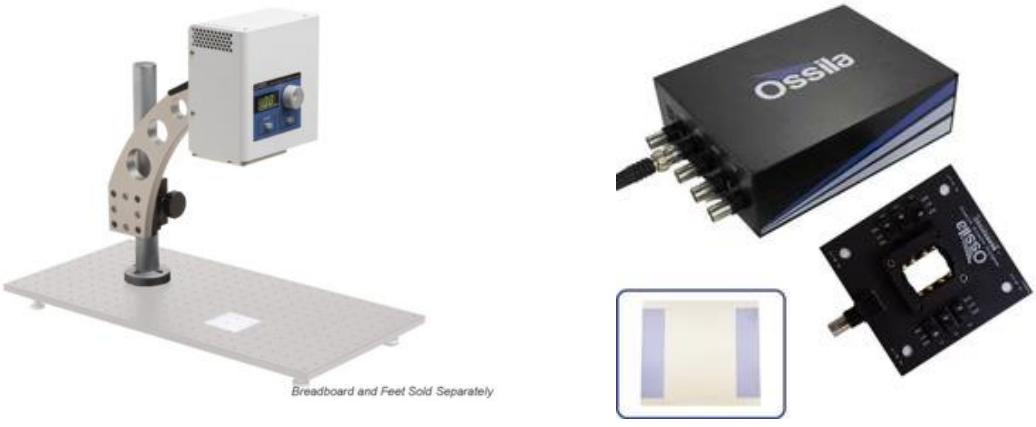

Figure 11.: Left) a LED based solar simulator. Right) Ossila Solar Cell I-V Test System (under) and UNIT-X200 Source Measure Unit (above).

J-V measurements are controlled by Ossila software and calibrated by a commercial silicon solar cell. Key measurement parameters are listed below: **Scan rate** (0.10-0.12 V/s.), **Step potential** (0.01 V). The devices were measured unencapsulated. A shadow mask was used to determine the illumination area of 0.0256 cm^2. The active area of the device is 3 cm^2 (FTO TEC8:20 mm x 15 mm).

3.3 STUDY OF MEMRISTOR BEHAVIOUR OF PHOTOVOLTAIC CELLS.

The cyclic voltammetry allows a qualitatively addressing of the memristive properties of the device. For the study of the memristive behavior of the developed perovskite solar cells, cyclic voltammetry (CV) is performed, both in dark conditions and 1sun illumination conditions. The instrumental equipment used for cyclic voltammetries is 'Autolab PGSTAT101' (Figure A6.), a potentiostat/galvanostat with a Compliance Voltage +10V, maximum current +100mA, which offers other standard electrochemical techniques. The instrument is controlled from a software 'NOVA 1.8' that allows configuring the main analysis parameters of cyclic voltammetry: **Upper vertex potential**: 1.0 V; **Lower vertex potential**: -1.0V; **Step potential**: 0.01V; **Scan rate**: 0.1 V/s; **Number of cycles**: 40. The perovskite solar cells are connected to the potentiostat through the same Ossila holder that we used for the J-V measurements (Figure 11. Right)).

3.4 CHARACTERIZATION OF CRYSTALLOGRAPHIC AND MORPHOLOGICAL PROPERTIES OF THE LAYERS BY STRUCTURAL CHARACTERIZATION TECHNIQUE.

To analyze the different layers from the perovskite solar cells, the following structural characterization technique have been carried out:

XRD: An Empyrean diffractometer from Panalytical performed powder XRD on samples using Cu Kα radiation (λ = 1.5406 Å) and a PIXcel-1DMedipix3 detector recording between 0 and 60° 2θ at a scan rate of 0.74°/min and 0.026° scan step. The sample holder was a silicon plate free of diffraction peak or shoulder rotating at 0.5 cycles per second to ensure uniformity in the detected signal.

4. RESULTS AND DISCUSSION

4.1 PV CHARACTERISTICS AND MEMRISTOR BEHAVIOUR

This section discusses the solar cell performance as well as the memristive behavior of the four above-mentioned structures developed in the project. For each structure, we have selected several devices and they will be named as follows. The devices with: FTO/c-SnO_2/MAPI/Spiro-OMeTAD/Au structure will be **samples 1-4**, FTO/c-SnO_2/m-TiO_2/MAPI/Spiro-OMeTAD/Au will be refereed as **samples 5-8**, FTO/c-TiO_2/MAPI/Spiro-OMeTAD/Au will be **samples 9-12**, and FTO/c-TiO_2/m-TiO_2/MAPI/Spiro-OMeTAD/Au will be named as **samples 13-16**.

FTO/c-SnO_2/MAPI/Spiro-OMeTAD/Au (samples 1-4)

The J-V curves of the **samples 1-4** were measured under 1 sun illumination and in dark conditions.

The PV parameters were extracted from the corresponding curve measured under light (Table A1, Annex). Due to the data spreading of the different studied devices, the average values for the PV parameters were calculated and presented in Table 1. To simplify, the results of **sample 1** (8.4 %

PCE, Figure 12) and **4** (4.1 % PCE, Figure 13) are presented in this section (see also the PV parameters in Table 1), being the most and lowest efficient PSCs with FTO/c-SnO_2/MAPI/Spiro-OMeTAD/Au structure, respectively. The J-V curves of **sample 2** (6.9 % PCE) and **3** (5.5 % PCE) are presented in Annexes (Figure A7 & Figure A8 and their PV parameters in Table A1).

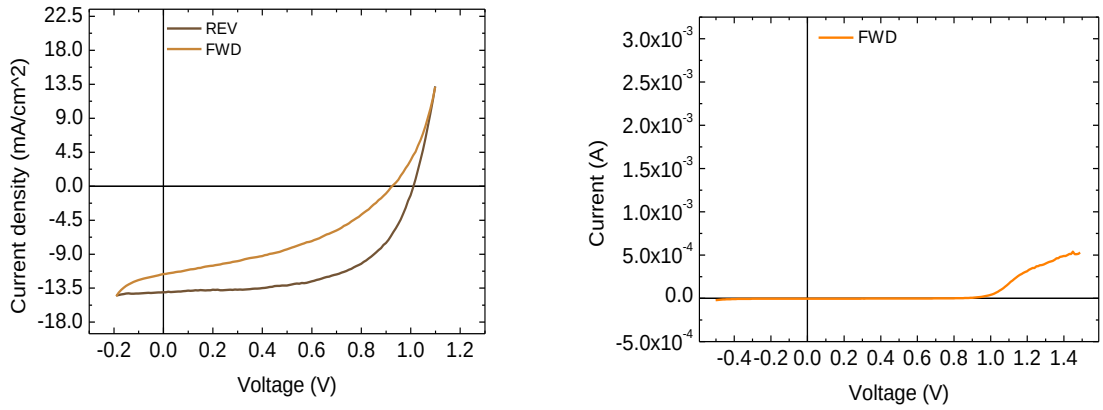

Figure 12.: **Sample 1**: Left) J-V curve measured under 1 sun illumination. Right) I-V curve in dark conditions

Sample 1 (PCE: 8.3%) shows the highest efficiency for the studied devices of this structure, especially due to its V_{oc} = 1.01 V but also because of its acceptable J_{sc} = 14.04 mA/cm^2 (REV scan direction). The parameter that avoids it to reach higher efficiencies is FF (59%), far from FF~86% of the best performing solar cell reported in the literature.[50] The low values of J_{sc} and FF can be originated by a non-ideal extraction of the photogenerated charge carriers by the charge transport layer.[50] This device shows lower performance in the forward scan (FWD) with PCE=3.1%, leading to a solar cell with a 0.63 hysteresis index (HI).

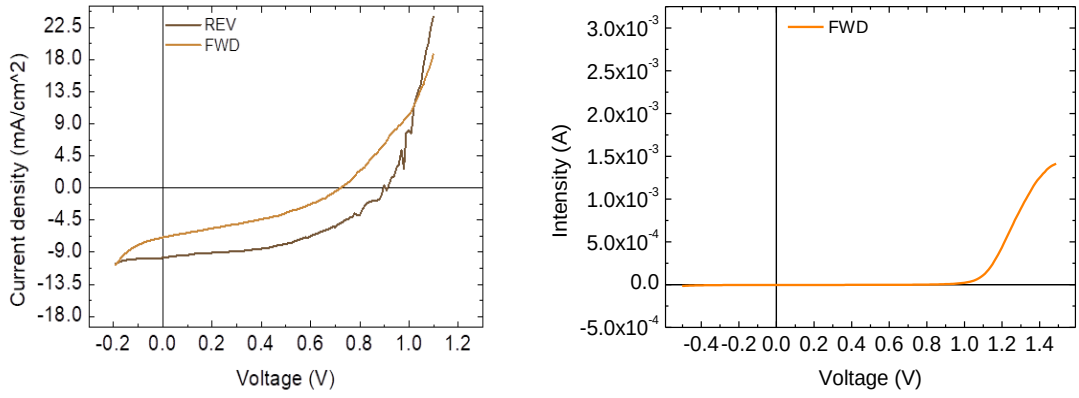

Figure 13.: **Sample 4:** Left) J-V curve under 1 sun illumination. Right) I-V curve dark conditions

Sample 4 shows the lowest efficiency for the studied devices of this structure with a PCE of 4.1%. In Figure 13.Left), V_{oc} = 0.90 V and J_{sc} = 9.76 mA/cm^2 can be seen, added to a FF = 47%, are the reasons for its low efficiency. The lower PV parameters in comparison to Sample 4 can be attributed

to a lower quality of the perovskite layer inducing higher charge recombination in the device with a lower V_{oc} value.[51] **Sample 4** has a HI of 0.56, being similar to the average values of this series. In spite of the low PV performance observed under illumination, the I-V curves measured under dark conditions (Figure 13.Right)) show and confirm the diode behavior of the fabricated and studied solar cells.

To study the memristive behavior, cyclic voltammetries (CVs) are first measured under dark conditions. In all the CVs presented in the work, 40 cycles are performed to study the stability over time. Only 1st, 20th and 40th cycles are presented so the changes in the stability can be clearly appreciated. In **samples 1-4** all the CV in dark conditions (Figures A10, A11 & A12) have an identical shape to the one shown in Figure A9. In which, a hysteresis loop at positive voltages is observed in the first cycle but in the 20th and 40th cycle the hysteresis is reduced.

When studying CV of **samples 1-4** under 1 sun illumination the shape of the curve is very different from the curves under dark conditions. The corresponding figure of merits (FOMs) and average values for **samples 1-4** characterized as memristors are presented in Table 1 and Table A1. The four samples present a similar behavior with a hysteresis loop at negative voltages and this shape can be seen in the first cycle specifically, from **sample 1** (best performing solar cell) and **sample 4** (worst performing solar cell). The CVs under 1 sun illumination of **sample 2** and **sample 3** are in the Annexes (Figure A13 and Figure A14).

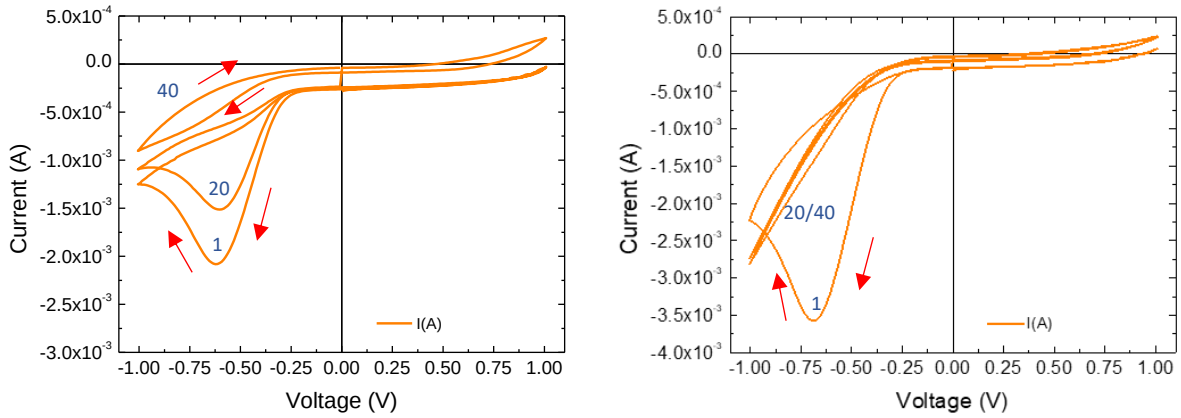

Figure 14.: Left) Cyclic voltammetry of **sample 1** under 1 sun illumination. Right) Cyclic voltammetry of **sample 4** under 1 sun illumination (Only cycle 1st, 20th and 40th are represented.)

In **sample 1,** in the first cycle of the CV a large hysteresis can be observed at negative voltages with an ON/OFF ratio of 2.59 (see Figure 14.Left)). The cycle has a bottle-shaped, rectification-mediated switching characteristic curve, with a V_{set} of -0.30 V and a V_{reset} of -0.63 V. The set and reset processes don't occur at opposite bias polarities, indicating that the device does not have bipolar RS

characteristics.[52] 40 cycles of CV were performed to analyse the stability of the memristive behaviour. As it can be seen in Figure 19, the memristive behaviour of **sample 1** is reduced at increasing number of CV cycles, with a transition from ON/OFF ratio from 2.59 (1st cycle) to an ON/OFF ratio of 0.33 (40th cycle) indicating that the memristive performance of this device layout is not stable in time.

The shape of the CV curve in **sample 4** (see Figure 14.Right)) is identical to the **samples 1 to 3** but with a much higher memristive behavior due to a higher ON/OFF ratio = 3.80, being the highest value of this series (see Table 1 for **samples 1 and 4** and Table A1 for all). Its V_{set} = -0.25 V and V_{reset} = -0.78 V show that the area where the maximum memristive behavior is studied extends over a wider range of voltages than **samples 1-3**. The memristive performance of this device is also not stable in time, losing the memristive behavior in the 20th cycle.

To sum up, in this device layout, a memristive behavior has been observed at negative voltages. There is a correlation between solar efficiency and memristive behavior, since the *Best performing solar cell* (**sample 1**) has a *much lower ON/OFF ratio* than the *worst performing solar cell* (**sample 4**) which has the *highest ON/OFF ratio*. Although a direct trend at increasing the memristor behaviour by decreasing photovoltaic device performance cannot be strictly determined -**sample 3** (PCE: 5.5%) has a lower ON/OFF ratio value (2.63) than **sample 2** (PCE: 6.9) (ON/OFF ratio = 3.49)- **as a general trend the memristive behavior increases at decreasing the solar cell performance.** Finally, the memristor behaviour for the devices with FTO/c-SnO_2/MAPI/Spiro-OMeTAD/Au layout is not stable over time, losing any trace of it when performing 40 cycles.

Table 1.: PV and memristor parameters of **sample 1**, **4** and average parameters.

	Solar Cell						Memristor			
	Scan direction	PCE (%)	J_{sc} (mA/cm^2)	V_{oc} (V)	FF (%)	HI	ON/OFF ratio	V_{set} (V)	V_{reset} (V)	Endurance time (40 cicles)
Best performing solar cell (**sample 1**)	*REV*	8.3	-14.04	1.01	59	0.63	2.59	-0.63	-0.30	NO
	FWD	3.1	-12.91	0.84	32					
Best performing memristor (**sample 4**)	*REV*	4.1	-9.76	0.90	47	0.56	3.80	-0.78	-0.25	NO
	FWD	1.8	-6.87	0.71	36					
Average (**samples 1-4**)	*REV*	6.2 ±1.8	-12.14 ± 1.86	0.96 ± 0.05	52 ± 6	0.63 ± 0.07	3.13 ± 0.61	-0.26 ± 0.06	-0.70 ± 0.03	NO
	FWD	2.8± 0.7	-10.33 ± 2.58	0.84 ± 0.08	34 ± 3					

.

- **FTO/c-SnO_2/m-TiO_2/MAPI/Spiro-OMeTAD/Au (sample 5-8)**

In this structure we have incorporated a mesoscopic TiO_2 layer between the SnO_2 and perovskite layers. Similar to the previous structure, the solar cell performance of this device layout is determined by measuring J-V curves under 1 sun illumination (parameters in Table A2) and in dark conditions. In view of the great heterogeneity of results, the results of **sample 5** (9.4 % PCE, Figure 15), **sample 6** (7.3 % PCE, Figure 16) and are presented in this section (see also the PV parameters in Table 2), being the two most efficient PSCs with FTO/c-SnO_2/m-TiO_2/MAPI/Spiro-OMeTAD/Au structure, respectively. The J-V curve of **sample 7** (2.5 % PCE) and **sample 8** (2.1% PCE,) are presented in Annexes (Figure A15 and Figure A16).

Sample 5 (PCE: 9.4%) shows the highest efficiency for the studied devices of this structure (also the highest of the devices of all the layouts) with J_{sc} = -15.13 mA/cm^2, FF = 66% and V_{oc} = 0.95V values in the reverse scan. Although the open-circuit voltage is lower than the previous layout (see **sample 1,** V_{oc} =1.01 V), the charge extraction is enhanced observed in the higher values for J_{sc} and FF in this device structure increasing the overall value of efficiency. The lower device performance obtained in the forward scan (FWD) with a 5.4% PCE leads to a hysteresis index parameter of 0.43, being lower value than for the previous layout (see Table 1, **sample 1** HI=0.63).

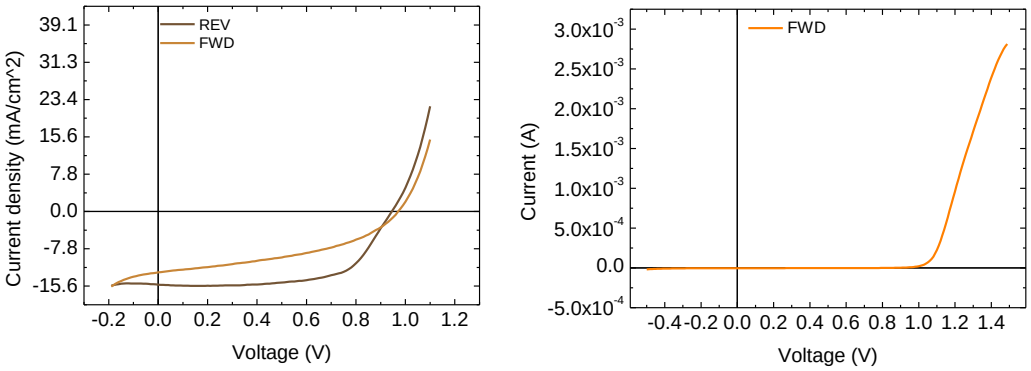

Figure 15.: **Sample 5:** Left) J-V curve under 1 sun illumination. Right) I-V curve dark conditions

Although J-V curve in **Sample 6** (PCE: 7.3 %), with FF = 64 % and V_{oc} = 0.97 V, has a similar shape to that of **Sample 5** its efficiency is 2% lower maybe due to a slight decrease in the charge extraction with a lower J_{sc} = 11.73 mA/cm^2. The hysteresis observed in **sample 5** is increased to HI=0.51 due to the lower efficiency obtained in the forward scan (FWD) (PCE: 3.6%). **Samples 7** (PCE: 2.5%) and **8** (PCE: 2.1%) considerably lower the solar efficiency, FOR instance, **Sample 8** has the lowest PV parameters of J_{sc} = -10.94 mA/cm^2, V_{oc} = 0.63 V and FF = 31% meaning a higher charge recombination and reduced charge extraction in the device.Although the solar cell performance is

low, the I-V curves under dark conditions (Figure 16.Right)) show and confirm the diode behavior of the fabricated and studied solar cells with FTO/c-SnO_2/m-TiO_2/MAPI/Spiro-OMeTAD/Au layout.

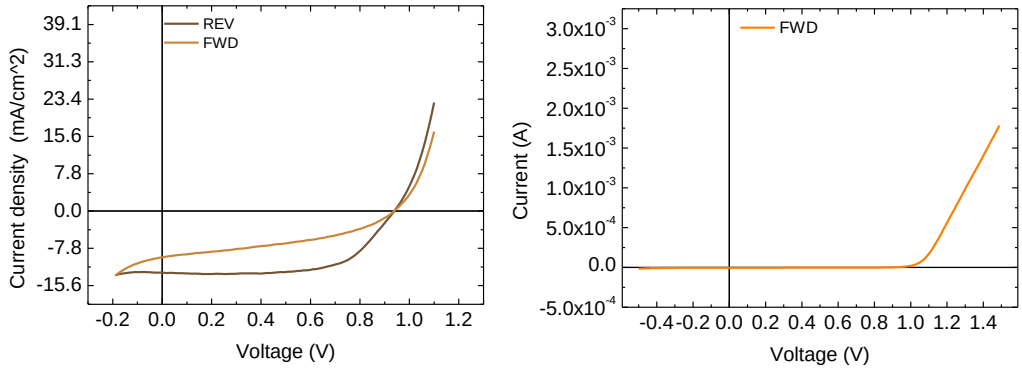

Figure 16.: **Sample 6:** Left) J-V curve under 1 sun illumination Right) I-V curve dark conditions

Cyclic voltammetries (CVs) are first measured under dark conditions. In **samples 5-7,** the CV in dark conditions Figure A17 for sample 6 and Figure A18 for sample 7) have an identical shape between them and to the one shown in Figure 17.Left)). Sample 8 is an exception as a hysteresis loop at positive voltages appears in the first cycle of the CV in dark conditions. But the hysteresis is reduced in cycles 20 and 40 (Figure 17.Right)).

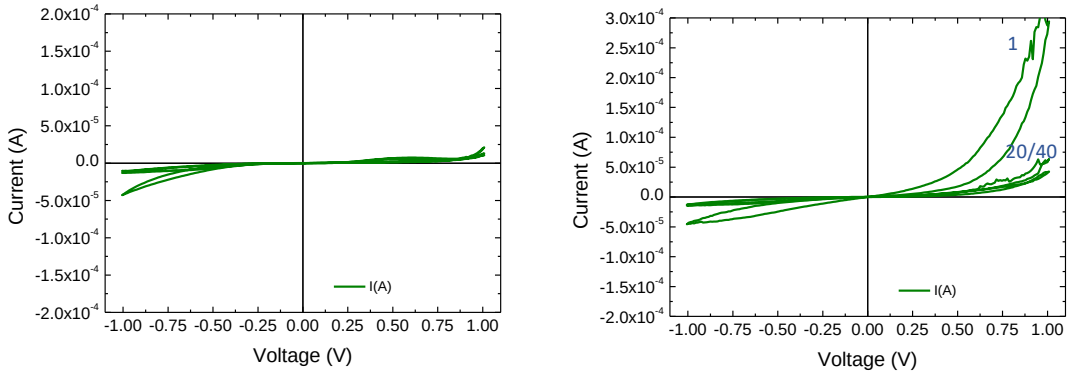

Figure 17.: Left) Cyclic voltammetry of **sample 5** in dark conditions Right) Cyclic voltammetry of **sample 8** in dark conditions.((Only cycle 1st, 20th and 40th are represented.)

When studying CV under 1 sun illumination two types of curves can be observed. **Samples 5, 6** (Figure 18.Left) and Figure A19) present a memristive behavior at negative voltages while **samples 7, 8** do not present any hysteresis in all voltammetry, showing curves without memristive behaviour (Figure18.Right) and Figure A20).

The curves of **samples 5,6** (Figure 18. Left) and figure A19) have a similar shape with the hysteretic cycle at negative voltages, so that, dispersion in the values of average (of **sample 5** and **sample 6**) V_{set} = -0.29 ± 0.01 V and V_{reset} = -0.82 ± 0.03 V is very low. These values demonstrate that set and reset processes don't occur at opposite bias polarities, indicating that the device layout does not have a bipolar RS characteristics.[52] For **Sample 5** (9.4%) ON/OFF ratio = 1.15 and **Sample 6** (PCE: 7.3%) shows ON/OFF ratio = 1.34, a difference in ON/OFF ratio that is not significant because it falls within the standard deviation of the mean, so no significant conclusions can be drawn from the PCE-ON/OFF correlation in samples 5-6.. **The ON/OFF ratio values show that the memristive behavior is much lower than the average of the structure FTO/c-SnO_2/MAPI/Spiro-OMeTAD/Au. Sample 7** (PCE: 2.5%) and **sample 8** (PCE: 2.1%)**,** whose voltammetries have no appreciable ON/OFF ratio, do show a **correlation in the sharp drop in PCE and ON/off ratio** with respect to **samples 5 and 6**.

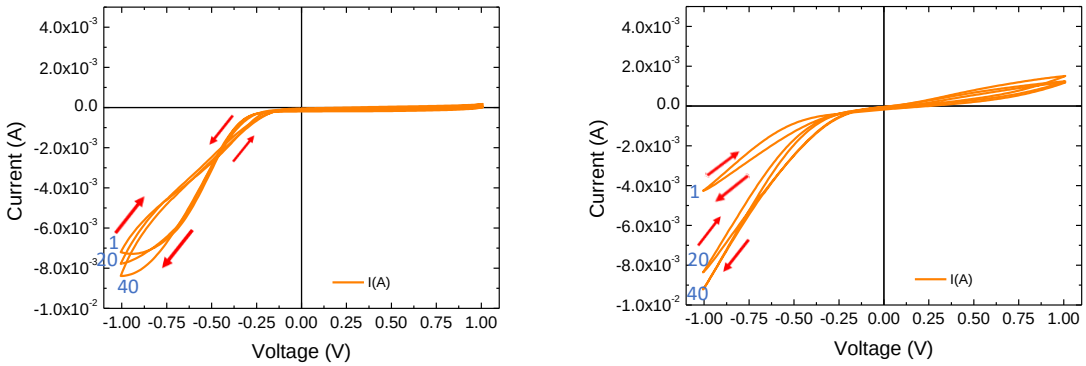

Figure 18.: Left) Cyclic Voltammetry of **Sample 5** under 1 sun illumination. Right) Cyclic Voltammetry of **Sample 8** under 1 sun illumination. (Only cycle 1st, 20th and 40th are represented.)

Table 2: PV and memristor parameters of **samples 5, 6** and average parameters. * For the memristor average only **sample 5 and sample 6** are considered.

	Solar Cell						Memristor			
	Scan direction	PCE (%)	J_{sc} (mA/cm^{-2})	V_{oc} (V)	FF (%)	HI	ON/OFF ratio	V_{set} (V)	V_{reset} (V)	Endurance time (40 cicles)
Best performing solar cell (**sample 5**)	*REV*	9.4	-15.13	0.95	66	0.43	1.15	-0.29	-0.80	YES
	FWD	5.4	-12.75	0.97	43					
Best performing memristor (**sample 6**)	*REV*	7.3	-11.73	0.97	64	0.51	1.34	-0.28	-0.84	YES
	FWD	3.6	-9.15	0.97	40					

Average (**of samples 5-8**)	*REV*	5.3 ±3.6	-11.85 ± 2.36	0.81 ± 0.17	50 ± 18	0.57± 0.13	1.25 ± 0.13	-0.29 ± 0.01	-0.82 ± 0.03	YES

- **FTO/c-TiO_2/MAPI/Spiro-OMeTAD/Au (sample 9-12)**

In this section, we will analyze the effect of only a c-TiO_2 layer as electron transport layer. The J-V curves of the **sample 9-12** were measured under 1 sun illumination and in dark conditions. The PV parameters were extracted from the corresponding curve measured under light (see Table A3). To simplify, the results of **sample 9** (champion device with 8.9 % PCE, Figure 19) and **sample 10** (second best device performance with 7.3 % PCE, Figure 20) are presented in this section (see also the PV parameters in Table 1). The J-V curves of **sample 11** (5.4 % PCE) and **12** (5.2 % PCE) are presented in Annexes (Figure A21 & Figure A22 and their PV parameters in Table A3.)

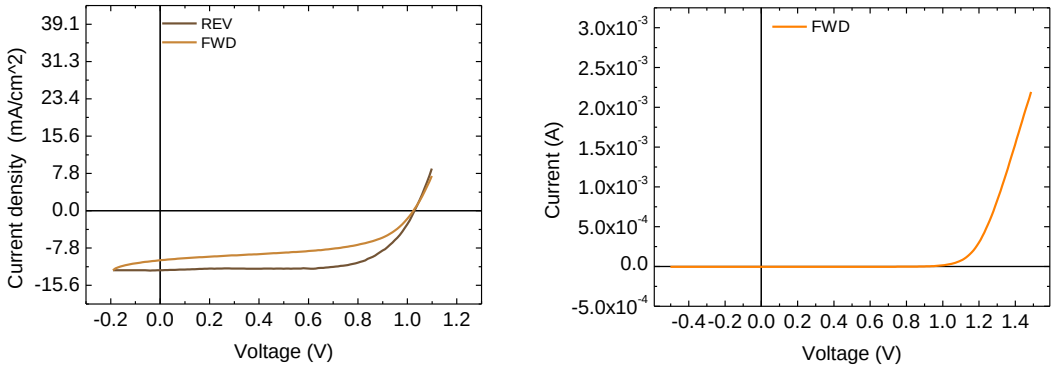

Figure 19.: **Sample 9:** Left) J-V curve under 1 sun illumination. Right) I-V curve dark conditions

Sample 9 (PCE: 8.7%) (see Figure 19) shows the highest efficiency for the studied devices of this structure, with adequate PV parameters in the reverse scan direction (REV): J_{sc} = -12.46 mA/cm^2 and V_{oc} = 1.03 V. As previously observed in the other device structures, the low J_{sc} and FF values avoid reaching higher efficiencies, indicating again charge extraction difficulties in the device.[50] The lower device performance obtained in the forward scan (FWD) with PCE= 5.7 % leads to a solar cell with a 0.36 hysteresis index (HI).

Sample 10 (PCE: 7.3%) is the second most efficient device of the series (see Figure 20). Although the shape of the curve is similar to **sample 9** (FF = 64% and 68% for **sample 10** and **9**, respectively), the drop in efficiency in sample 10 is due to the worsening of the J_{sc} and V_{oc} parameters (J_{sc} = -11.73 mA/cm^2 and V_{oc} = 0.97 V), indicating higher charge recombination in the device. The HI is higher (HI = 0.51) because the measurement performed at forward scan suffers a sharp drop (PCE: 4.6%).

Sample 12 (PCE: 5.2%) (Figure A22) has an appropriate rectification behavior with a curve shape (FF = 62%), similar to the already studied samples of this structure, while **sample 11** (PCE: 5.4 %) (Figure A21) is considerably unlike due to the lower FF values. These differences will affect

to the memristive behavior.

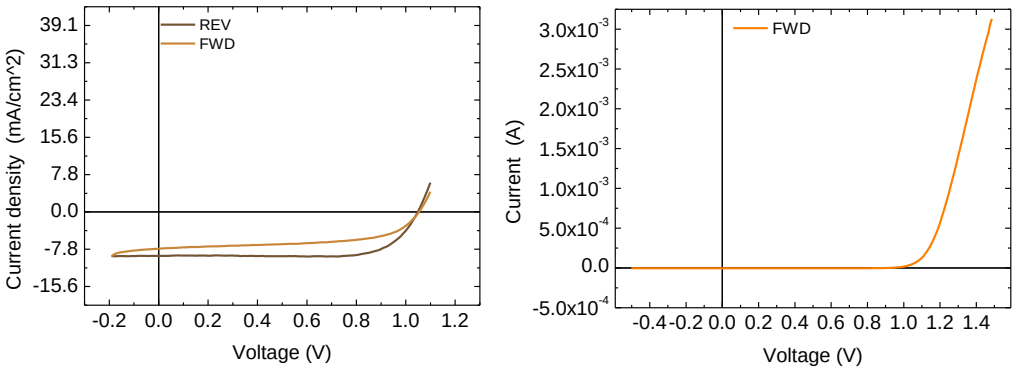

Figure 20.: **Sample 10:** a) J-V curve under 1 sun illumination b) I-V curve dark conditions

Cyclic voltammetries (CVs) are first measured under dark conditions. **Sample 9** (Figure 21. Left) shows different features in dark conditions with the appearance of a memristive loops at positive and negative bias. These features are not observed in the rest of the samples of this series (see Figure 21.Right), A23 and A24) as they present voltammetries without any any hysteresis loop.

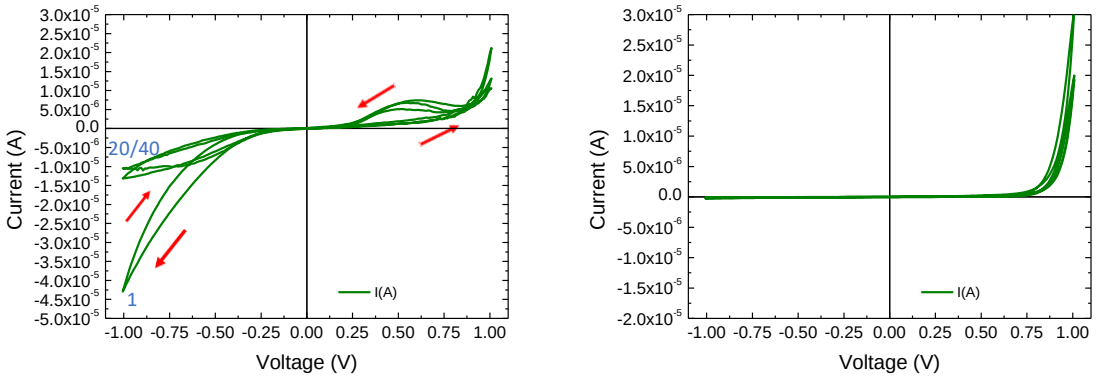

Figure 21.: Left) Cyclic voltammetry of **sample 9** in dark conditions Right) Cyclic voltammetry of **sample 10** in dark conditions (Only cycle 1st, 20th and 40th are represented.)

When studying CV under 1 sun illumination one type of curves can be observed. The curves of **samples 9**, **10 and 12** (Figure 22 and figure A25) have a similar shape with the hysteretic cycle at positive and negative voltages, therefore, their voltammetric curves take on a bottle shape. The dispersion in the average set voltage values V_{set} = 0.79 ± 0.03 V is very low. The ON/OFF ratio

values show that the memristive behavior is low (1.42 ± 0.12). In this structure the memristive behavior increases with cycles.

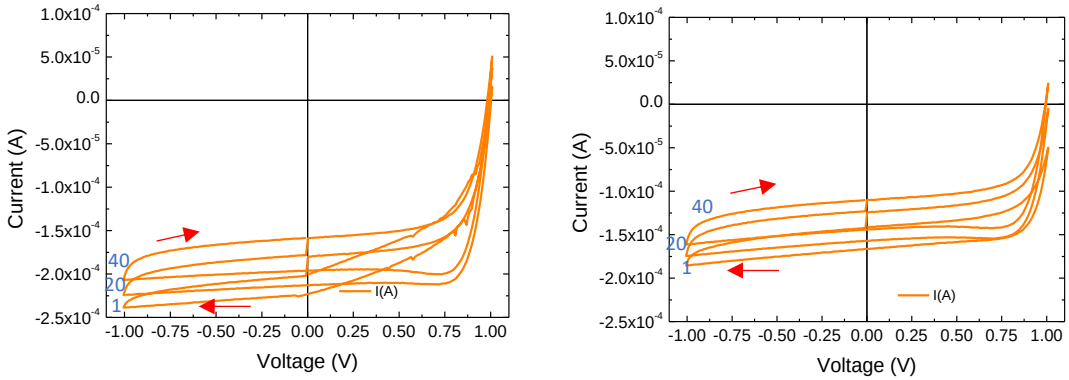

Figure 22.: Left) Cyclic voltammetry of **sample 9** under 1 sun illumination Right) Cyclic voltammetry of **sample 10** under 1 sun illumination (Only cycle 1st, 20th and 40th are represented.)

Sample 11 is an exception because it does not show memristive behavior (see Figure A26). The PV parameters of **sample 11** (PCE: 5.4%, FF = 56 %, V_{oc} = 0.93 V and HI = 0.48) stand out as being different from the average parameters of this structure (consult average data in Table3). Perhaps this disparity of parameters can be correlated with the null memristive behavior of the sample.

In this device layout, a memristive behavior has been observed along the reading voltage, associated with the bottle-shaped behaviour of the **Sample 9, Sample 10** and **Sample 12** curves. It cannot be associated a correlation between solar efficiency and memristive behavior in this device layout, since the Best performing solar cell **Sample 9** (PCE: 8.9%) has a memristor ON/OFF ratio = 1.45 while **Sample 10** (PCE: 7.3%) show an ON/OFF ratio = 1.52 and the worst performing solar cell **Sample 12** (PCE: 5.2 %) just an ON/OFF ratio = 1.29 (see Table A3). To clarify, as the second sample with higher PCE (**Sample 12**) has better memristive behaviour than **sample 9** and **sample 12** (with higher and lower PCE respectively) there is no link between PCE and memristive behaviour (ON/OFF ratio). Furthermore, the differences in ON/OFF ratio between the samples fall within the standard deviation and are therefore not significant differences to draw conclusion.

Table 3: PV and memristor parameters of sample 9, 10 and average parameters. *The memristor behaviour of sample 11 is not evaluated in this table.

	Solar Cell						Memristor*			
	Scan direction	PCE (%)	J_{sc} (mA/cm^2)	V_{oc} (V)	FF (%)	HI	ON/OFF ratio	V_{set} (V)	V_{reset} (V)	Endurance time (40 cicles)
Best performing	*REV*	8.9	-12.46	1.03	68					

solar cell (**sample 9**)	*FWD*	5.7	-10.32	1.01	54	0.36	1.45	0.79	-	YES (Increase with Cycles)
Best performing memristor (**sample 10**)	*REV*	7.3	-11.73	0.97	64	0.51	1.52	0.80	-	YES (Increase with cycles)
	FWD	4.6	-9.15	0.97	40					
Average (**samples 9-12**)	*REV*	6.7 ± 1.8	-10.05 ± 2.37	1.01 ± 0.05	63 ± 5	0.40± 0.06	1.42 ± 0.12	0.79 ± 0.03	-	YES (Increase with cycles)
	FWD	4.08 ± 1.33	-8.17 ± 1.76	0.95 ± 0.15	52 ± 5					

- **FTO/c-TiO_2/m-TiO_2/MAPI/Spiro-OMeTAD/Au (Samples 13-16).**

The last device structure is formed by a compact and mesoporous TiO_2 bilayer as electron transport layers. The J-V curves of the **samples 13-16** were measured under 1 sun illumination and in dark conditions. The PV parameters were extracted from the corresponding curves measured under light. Results of **sample 13** (8.4 % PCE, Figure 23), **sample 14** (4.1 % PCE, Figure 24) are presented in Table 4, additional data for **sample 15** (2.9% PCE, Figure A27) and **sample 16** (2.5 % PCE, Figure A28) are in Table A4.

Sample 13 (PCE: 4.7 %) shows the highest efficiency for the studied devices of this structure. Despite the very low J_{sc} = -7.49 mA/cm^2 value, the parameters V_{oc} = 0.98 V and FF = 64 % make it possible to increase efficiency (see Figure 23). The low J_{sc} might be originated by issues in the perovskite layer but still adequate charge extraction (reasonable V_{oc} and FF values). The lower device performance obtained in the forward scan (FWD) with PCE=2.4 % leads to a solar cell with a 0.49 hysteresis index (HI).

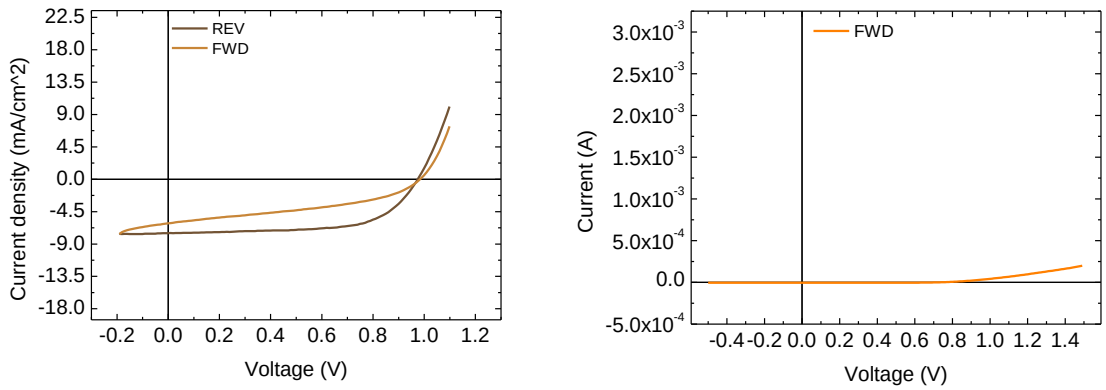

Figure 23.: **Sample 13**: Left) J-V curve under 1 sun illumination. Right) I-V curve dark conditions

Sample 14 (PCE: 4.3%) has a similar efficiency to **sample 13** even though the shape of the J-V curve is very different (see Figure 24), with a FF = 57 %, a greater J_{sc} = -12.42 mA/cm^2 but a worse

V_{oc} = 0.96 V. 0.51 hysteresis index (HI) shows that forward scan (FWD) direction achieves lower efficiency (2.1 % PCE). The I-V curves under dark conditions (Figure 24.Right) show and confirm the diode behavior of the fabricated and studied solar cells.

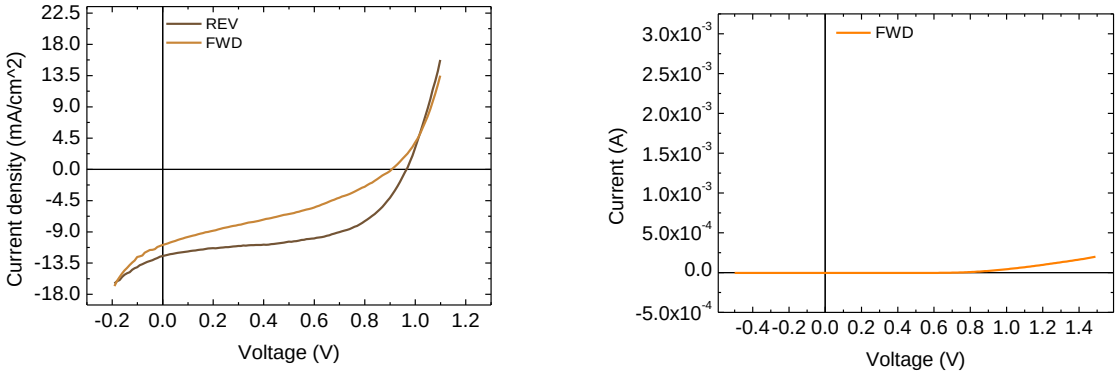

Figure 24.: **Sample 14**: Left) J-V curve under 1 sun illumination. Right) I-V curve dark conditions

Cyclic voltammetries (CVs) are first measured under dark conditions. In **sample 13-15** the CV in dark conditions (Figure 25, Figure A29) the shape is identical (diode shape). The CV of sample 16 has a different shape with the appearance of a hysteresis loop with little intensity (see Figure A30).

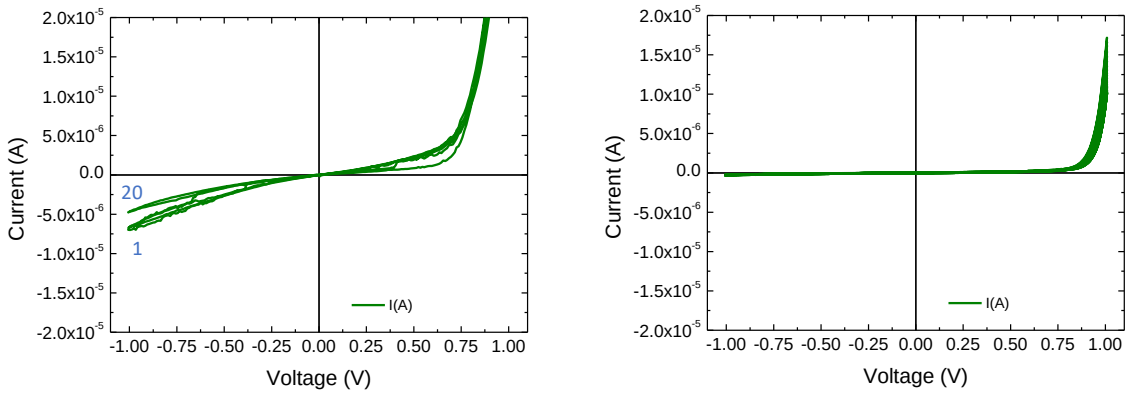

Figure 25.: Left) Cyclic voltammetry of **sample 13** in dark conditions. **Right)** Cyclic voltammetry of **sample 14** in dark conditions. (Only cycle 1st, 20th and 40th are represented.)

When studying CV under 1 sun illumination the curves of all the samples have very similar shapes, like a 'hysteresis loop'. The 4 sample curves have only one V_{set}, with an average of **V_{set} = 0.72 ± 0.05 V** (Table 4) but no V_{reset} is visible so that this device layout does not have a bipolar RS characteristics[2]. The average **ON/OFF ratio** = 2.62 ± 0.97 is a high value compared to other layouts, with a large dispersion due to the following reason: **samples 13 and 14** with PCE ≈ 4 % have an ON/OFF ratio of more than 3 (see Figure 26), while the **samples 15 and 16** (Figure A31 and Figure A32 respectively) with PCE = 2.5-3 % set the ON/OFF ratio = 1.5-2.2. In this device layout **there is a direct proportional relationship between the PCE and the ON/OFF Ratio** (solar efficiency and memristive behaviour). Finally, the samples withstand the application of the 40 cycles without clearly modifying their memristive behaviour.

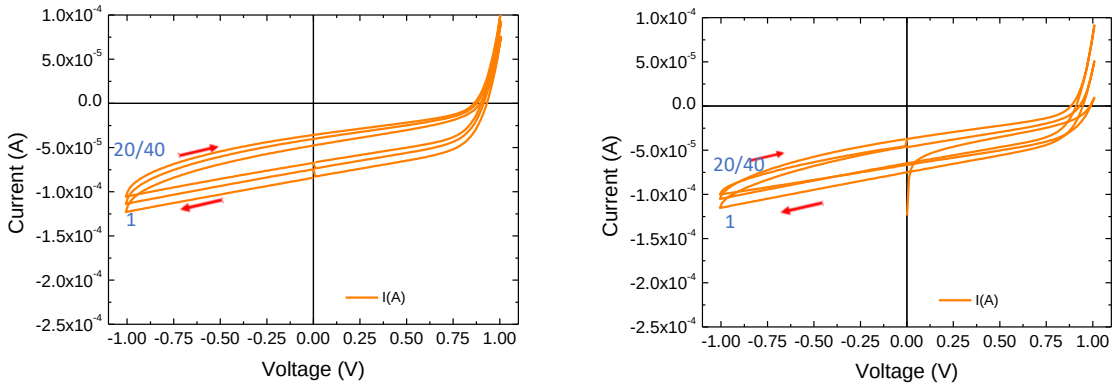

Figure 26.: Left) Cyclic Voltammetry of **Sample 13** under 1 sun illumination. Right) Cyclic Voltammetry of **Sample 14** under 1 sun illumination. (Only cycle 1st, 20th and 40th are represented.)

Table 4: PV and memristor parameters of **sample 13**, **sample 14** and average parameters.

	Solar Cell						Memristor z			
	Scan direction	PCE (%)	J_{sc} (mA/cm^{-2})	V_{oc} (V)	FF (%)	HI	ON/OFF ratio	V_{set} (V)	V_{reset} (V)	Endurance time (40 cicles)
Best performing solar cell **(sample 13)**	REV	4.7	-7.49	0.98	64	0.49	3.07	0.68	-	YES
	FWD	2.4	-6.08	0.97	41					
Best performing memristor **(sample 14)**	*REV*	4.3	-12.42	0.96	57	0.51	3.7	0.78	-	YES
	FWD	2.1	-10.82	0.90	31					
Average	*REV*	3.6 ± 1.0	-10.22 ± 4.90	0.96± 0.04	58 ± 8	0.36 ± 0.16	2.62 ± 0.97	0.72 ± 0.05	-	YES
	FWD	2.2 ± 0.2	8.48 ± 4.29	0.93 ± 0.06	38 ± 7					

Finally, a summary of the average values (see Table A5) of each structure is presented with the characteristics of each structure:

- *FTO/c-SnO_2/MAPI/Spiro-OMeTAD/Au*: an average **PCE = 6.2 ±1.8** places this structure as the second with highest average solar efficiency of those studied the one with the highest hysteresis index (**HI = 0.63± 0.07)**. In terms of memristive behaviour, all four samples have bottle-shaped voltammetries, rectification-mediated switching characteristic curve, with an average **Vset = -0.26 ± 0.06 V** and a **Vreset = -0.70 ± 0.03 V**. In this device layout, the highest average **ON/OFF ratio = 3.13 ± 0.61** is observed as well as a *correlation in which the memristive behavior increases at decreasing the solar cell performance*. The negative note comes with the loss of stability when performing the 40 cycles.
- *FTO/c-SnO_2/m-TiO_2/MAPI/Spiro-OMeTAD/Au:* This device layout has the second worst average value of **PCE = 5.3 ±3.6 %** however, the device with the highest PCE of all those studied in the project is of this structure (**Sample 5, PCE = 9.4%**), showing the great heterogeneity in solar cell parameters. The average memristive behaviour (**ON/OFF ratio= 1.25 ± 0.13**) is much lower than the previous structure and only exists in 2 of the 4 devices studied. Coincidentally, **samples 7** and **8** with much lower PCEs (have no memrsitive behaviour so there could be a diffuse trend towards *lower PCE, lower ON/OFF ratio*.
- *FTO/c-TiO_2/MAPI/Spiro-OMeTAD/Au:* With an average **PCE = 6.7 ± 1.8 %** is the device layout with the best average solar efficiency and a lower hysteresis index than the two previous layouts (**HI = 0.40± 0.06**). Their memristive behaviour is different because, despite the fact that the voltammetries take on a bottle shape, only present a V_{set} = 0.79 ± 0.03 V and **they lack V_{reset}** as well as a small **ON/OFF ratio = 1.42 ± 0.12** compared to other layouts. They are stable over the 40 cycles and an increase in memristive behaviour is even observed. No general trends in correlation of PCE-memristic behaviour.
- *FTO/c-TiO_2/m-TiO_2/MAPI/Spiro-OMeTAD/Au:* Based on solar efficiency, it is the worst device layout (average **PCE = 3.6 ± 1.0 %)** and has the lowest hysteresis index **(HI = 0.36 ± 0.16).** About memristive behaviour, the shape of the voltammetries is similar to that of the '*c-TiO_2*' (**V_{set} = 0.72 ± 0.05 V, no V_{reset}**) layout but with a higher average **ON/OFF ratio = 2.62 ± 0.97.** The memristive behaviour remains stable after 40 cycles.

For comparison, a 40-cycle voltammetry was performed under 1 sun illumination on a reference cell in particular, a Silicon PV (Figure A32). The reading voltage is: **Upper vertex potential:** 0.4 V; **Lower vertex potential**: -0.7V to guarantee the non-rupture of the cell. In Figure A33, it can be seen

how a reference cell prepared to have no hysteresis behaves in the voltammetries, without any memristive behaviour. This behaviour is very different from the devices studied in this project.

5. CHARACTERIZATION.

XRD: A structural characterisation by XRD of an FTO device with a deposited (by spin coating) MAPI perovskite layer (without any other layer) is carried out to check whether the perovskite film was acquiring the right orientation and whether impurities were present (see Figure A34). XRD analysis shows the characteristic peaks of 3D-MAPI (*110 at* 2θ = 14.2º*, 202 at* 2θ = 24.0º *,220 at* 2θ = 28.5º *, 310 at* 2θ = 31.8º*, 224 at* 2θ = 40.5º*, 330* at 42.9º)[55] crystal planes of the tetragonal phase so the formation of spin-coated PVK film is correct. However, peaks associated with the presence of PbI_2 (*001* at 2θ = 12.7º, *002* at 2θ = 24.6º),[55] i.e. unreacted reagent present in the PVK film, are observed, which may affect the performance of the device.

6. CONCLUSIONS.

After the completion of this Final Master Project, the conclusions drawn are as follows:

- ✓ The methods developed for the manufacture of PSCs are successful and achieve the goal of creating functional solar cells.
- ✓ Four different device layouts have been developed and their behaviour as photovoltaic cells and their memristive behaviour have been studied.
- ✓ Correlation trends of solar efficiency with memristive behaviour have been found in only two of the four structures studied: 1)*FTO/c-SnO_2/m-TiO_2/MAPI/Spiro-OMeTAD/Au*, in which, **the memristive behavior increases at decreasing the solar cell performance** and 2) *FTO/c-TiO_2/m-TiO_2/MAPI/Spiro-OMeTAD/Au*, in which, there is a direct proportional relationship between the PCE and the ON/OFF Ratio.

7. REFERENCES

1. Tian, J., Xue, Q., Yao, Q., Li, N., Brabec, C. J., & Yip, H. L. (2020). Inorganic halide perovskite solar cells: progress and challenges. *Advanced energy materials*, 10(23), 2000183**.**
2. Basumatary, P., & Agarwal, P. (2022). A short review on progress in perovskite solar cells. *Materials Research Bulletin*, 149, 111700.
3. Wang, D., Wright, M., Elumalai, N. K., & Uddin, A. (2016). Stability of perovskite solar cells. *Solar Energy Materials and Solar Cells*, 147, 255–275.
4. Shahbazi, M., & Wang, H. (2016). Progress in research on the stability of organometal perovskite solar cells. *Solar Energy*, 123, 74–87.
5. Yin, X., Guo, Y., Liu, J., Chen, P., Chen, W., Que, M., Yang, Y. (2017). Moisture annealing effect on $CH_3NH_3PbI_3$ films deposited by solvent engineering method. *Thin Solid Films*, 636, 664–670.
6. Best Research-Cell Efficiency Chart. Accessed June 26, 2023. https://www.nrel.gov/pv/cell-efficiency.html
7. J. Bisquert and E. J. Juarez-Perez. (2019). The Causes of Degradation of Perovskite Solar Cells *J. Phys. Chem. Lett*. 10, 5889-5891
8. E. J. Juarez-Perez and M. Haro. (2020). Perovskite solar cells take a step forward *Science*, 368, 1309-1309
9. Ren, P., Sun, C., Shi, Y., Song, P., Yang, Y., & Li, Y. (2019). Global performance evaluation of solar cells using two models: from charge-transfer and recombination mechanisms to photoelectric properties. *Journal of Materials Chemistry C*, 7(7), 1934-1947.
10. Jha, A. R. (2009). Solar cell technology and applications. CRC press.
11. Perovskite solar cells: why they're the future of solar power. Solar Reviews. Accessed June 25, 2023. https://www.solarreviews.com/blog/are-perovskite-solar-cells-the-future-of-solar-power
12. Hussain, I., Tran, H.P., Jaksik, J. et al. (2018). Functional materials, device architecture, and flexibility of perovskite solar cell. *Emergent mater*. 1, 133–154
13. M. Saliba, T. Matsui, K. Domanski, J.-Y. Seo, A. Ummadisingu, S.M. Zakeeruddin, J.-P. Correa-Baena, W.R. Tress, A. Abate, A. Hagfeldt, M. Grätzel. (2016). Incorporation of rubidium cations into perovskite solar cells improves photovoltaic performance. *Science,* 354(6309), 206–209.
14. Baena, J. P. C., Steier, L., Tress, W., Saliba, M., Neutzner, S., Matsui, T., ... & Hagfeldt, A. (2015). Highly efficient planar perovskite solar cells through band alignment engineering. *Energy & Environmental Science*, 8(10), 2928-2934.
15. Song, Z., Watthage, S. C., Phillips, A. B., & Heben, M. J. (2016). Pathways toward high-performance perovskite solar cells: review of recent advances in organo-metal halide perovskites for photovoltaic applications. *Journal of photonics for energy*, 6(2), 022001-022001.
16. Solar Energy Technologies Office. (2018). Perovskite Solar Cells. Energy.gov. https://www.energy.gov/eere/solar/perovskite-solar-cells
17. Lee, S., Noh, J. H., Bae, S.-T., Cho, I.-S., Kim, J. Y., Shin, H., … Hong, K. S. (2009). Indium−Tin−Oxide-Based Transparent Conducting Layers for Highly Efficient Photovoltaic Devices. *The Journal of Physical Chemistry C*, 113(17), 7443–7447.

18. Yang, C.-H., Lee, S.-C., Chen, S.-C., & Lin, T.-C. (2006). The effect of annealing treatment on microstructure and properties of indium tin oxides films. *Materials Science and Engineering: B*, 129(1-3), 154–160.
19. Song S, Kang G, Pyeon L, et al. Systematically Optimized Bilayered Electron Transport Layer for Highly Efficient Planar Perovskite Solar Cells (η = 21.1%). *ACS Energy Letters*. 2017;2(12):2667-2673.
20. Jiang, Q., Zhang, X., & You, J. (2018). SnO2: a wonderful electron transport layer for perovskite solar cells. *Small*, 14(31), 1801154.
21. You, J., Hong, Z., Yang, Y., Chen, Q., Cai, M., Song, T. B., ... & Yang, Y. (2014). Low-temperature solution-processed perovskite solar cells with high efficiency and flexibility. *ACS nano*, 8(2), 1674-1680.
22. Lin, L., Jones, T. W., Yang, T. C. J., Duffy, N. W., Li, J., Zhao, L., ... & Wilson, G. J. (2021). Inorganic electron transport materials in perovskite solar cells. *Advanced Functional Materials*, 31(5), 2008300.
23. Luo, J., Wang, Y., & Zhang, Q. (2018). Progress in perovskite solar cells based on ZnO nanostructures. *Solar Energy*, 163, 289-306.
24. Zhang, P., Wu, J., Zhang, T., Wang, Y., Liu, D., Chen, H., ... & Li, S. (2018). Perovskite solar cells with ZnO electron-transporting materials. *Advanced Materials*, 30(3), 1703737.
25. Dunlap-Shohl, W. A., Younts, R., Gautam, B., Gundogdu, K., & Mitzi, D. B. (2016). Effects of Cd diffusion and doping in high-performance perovskite solar cells using CdS as electron transport layer. *The Journal of Physical Chemistry C*, 120(30), 16437-16445.
26. Rai, S., Pandey, B. K., & Dwivedi, D. K. (2020). Device simulation of low cost HTM free perovskite solar cell based on TiO2 electron transport layer. *3RD INTERNATIONAL CONFERENCE ON CONDENSED MATTER AND APPLIED PHYSICS* (ICC-2019).
27. Tavakoli, M. M., Tavakoli, R., Yadav, P., & Kong, J. (2019). A graphene/ZnO electron transfer layer together with perovskite passivation enables highly efficient and stable perovskite solar cells. *Journal of Materials Chemistry A*, 7(2), 679-686.
28. Chen, J. Q., Yang, D. H., Jiang, J. H., Ma, A. B., Song, D., Chao, Y. N., & Hu, M. Z. (2015). Research process of electron transport layer materials in composite perovskite solar cells. *Mater Rev*, 29(05), 1.
29. Min, H., Lee, D. Y., Kim, J., Kim, G., Lee, K. S., Kim, J., ... & Il Seok, S. (2021). Perovskite solar cells with atomically coherent interlayers on SnO2 electrodes. *Nature*, 598(7881), 444-450.
30. Dou, X., Sabba, D., Mathews, N., Wong, L. H., Lam, Y. M., & Mhaisalkar, S. (2011). Hydrothermal Synthesis of High Electron Mobility Zn-doped SnO2Nanoflowers as Photoanode Material for Efficient Dye-Sensitized Solar Cells. *Chemistry of Materials*, 23(17), 3938–3945.
31. Giovanni, David. (2017). Optical-spin dynamics in organic-inorganic lead halide perovskites. *Nanyang Technological University*.
32. Tian, W., Zhao, C., Leng, J., Cui, R., & Jin, S. (2015). Visualizing carrier diffusion in individual single-crystal organolead halide perovskite nanowires and nanoplates. *Journal of the American Chemical Society*, 137(39), 12458-12461.
33. Wehrenfennig, C., Eperon, G. E., Johnston, M. B., Snaith, H. J., & Herz, L. M. (2014). High charge carrier mobilities and lifetimes in organolead trihalide perovskites. *Advanced materials*, 26(10), 1584-1589.

34. Zhang, Z., Wei, D., Xie, B., Yue, X., Li, M., Song, D., & Li, Y. (2015). High reproducibility of perovskite solar cells via a complete spin-coating sequential solution deposition process. *Solar Energy*, 122, 97-103.
35. Mathies, F., Eggers, H., Richards, B. S., Hernandez-Sosa, G., Lemmer, U., & Paetzold, U. W. (2018). Inkjet-printed triple cation perovskite solar cells. *ACS Applied Energy Materials*, 1(5), 1834-1839.
36. Wang, P., Wu, Y., Cai, B., Ma, Q., Zheng, X., & Zhang, W. H. (2019). Solution-processable perovskite solar cells toward commercialization: Progress and challenges. *Advanced Functional Materials*, 29(47), 1807661.
37. Gonzalez-Pedro, V., Juarez-Perez, E. J., Arsyad, W. S., Barea, E. M., Fabregat-Santiago, F., Mora-Sero, I., & Bisquert, J. (2014). General working principles of $CH_3NH_3PbX_3$ perovskite solar cells. *Nano letters*, 14(2), 888-893.
38. Thomson, S. (2018). Measuring Charge Carrier Lifetime in Halide Perovskite Using Time-Resolved Photoluminescence Spectroscopy. *Edinburgh Instruments*, 23.
39. Rombach, F. M., Haque, S. A., & Macdonald, T. J. (2021). Lessons learned from spiro-OMeTAD and PTAA in perovskite solar cells. *Energy & Environmental Science*, 14(10), 5161-5190.
40. Wang, S.; Sina, M.; Parikh, P.; Uekert, T.; Shahbazian, B.;Devaraj, A.; Meng, Y. S. (2016) Role of 4-Tert-Butylpyridine as a HoleTransport Layer Morphological Controller in Perovskite Solar Cells. *Nano Lett*. 16, 5594−5600.
41. Klipfel, N., Kanda, H., Sutanto, A. A., Mensi, M., Igci, C., Leifer, K., ... & Nazeeruddin, M. K. (2021). Mechanistic Insights into the Role of the Bis (trifluoromethanesulfonyl) imide Ion in Coevaporated p–i–n Perovskite Solar Cells. *ACS Applied Materials & Interfaces*, 13(44), 52450-52460.
42. A. Abate, D. R. Staff, D. J. Hollman, H. J. Snaith and A. B. Walker, Influence of ionizing dopants on charge transport in organic semiconductors, *Phys. Chem*., 2014, 16, 1132–1138
43. Liang, L., Cai, Y., Li, X., Nazeeruddin, M. K., & Gao, P. (2018). All that glitters is not gold: Recent progress of alternative counter electrodes for perovskite solar cells. *Nano Energy*, 52, 211-238.
44. Khudayer, I. H. (2017). Study of Physical and Optoelectronic Properties of CuInSe2/Si Heterojunction Solar Cells. *Energy Procedia*, 119, 507–517.
45. PVEducation. Accessed June 27, 2023 https://www.pveducation.org/pvcdrom/solar-cell-operation/iv-curve
46. Chua, L. (1971). Memristor-The missing circuit element. *IEEE Transactions on Circuit Theory*, 18(5), 507–519.
47. Xu, W., Wang, J., & Yan, X. (2021). Advances in memristor-based neural networks. *Frontiers in Nanotechnology*, 3, 645995.
48. Al-Shidaifat, A., Chakrabartty, S., Kumar, S., Acharjee, S., & Song, H. (2020). A Novel Characterization and Performance Measurement of Memristor Devices for Synaptic Emulators in Advanced Neuro-Computing. *Micromachines*, 11(1), 89.
49. Berruet, M., Pérez-Martínez, J. C., Romero, B., Gonzales, C., Al-Mayouf, A. M., Guerrero, A., & Bisquert, J. (2022). Physical model for the current–voltage hysteresis and impedance of halide perovskite memristors. *ACS Energy Letters*, 7(3), 1214-1222.

50. Cao, Q., Li, Y., Zhang, H., Yang, J., Han, J., Xu, T., ... & Grätzel, M. (2021). Efficient and stable inverted perovskite solar cells with very high fill factors via incorporation of star-shaped polymer. *Science Advances*, 7(28), eabg0633.
51. Siekmann, J., Kulkarni, A., Akel, S., Klingebiel, B., Saliba, M., Rau, U., & Kirchartz, T. (2023). Characterizing the Influence of Charge Extraction Layers on the Performance of Triple-Cation Perovskite Solar Cells. arXiv preprint arXiv:2302.05749.
52. Li, D., Wu, B., Zhu, X., Wang, J., Ryu, B., Lu, W. D., ... & Liang, X. (2018). MoS_2 memristors exhibiting variable switching characteristics toward biorealistic synaptic emulation. *ACS nano*, 12(9), 9240-9252.
53. Cao, G., Cheng, C., Zhang, H., Zhang, H., Chen, R., Huang, B., … Chen, H. (2020). The application of halide perovskites in memristors. *Journal of Semiconductors,* 41(5), 051205.
54. Iwahara, H. (2009). Ionic conduction in perovskite-type compounds. *Perovskite oxide for solid oxide fuel cells*, 45-63.
55. Bahtiar, A., Rahmanita, S., & Inayatie, Y. D. (2017). Pin-Hole Free Perovskite Film for Solar Cells Application Prepared by Controlled Two-Step Spin-Coating Method. *IOP Conference Series: Materials Science and Engineering*, 196, 012037

ANNEXES

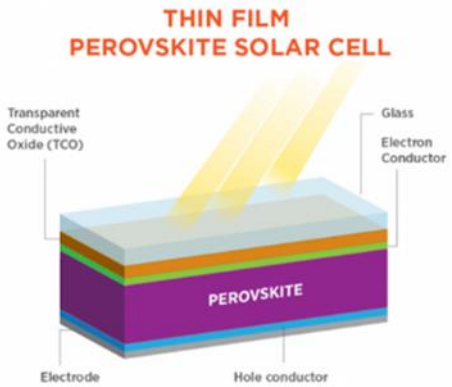

Figure A1.: Thin-film n-i-p perovskite solar cell (PSCs)[16]

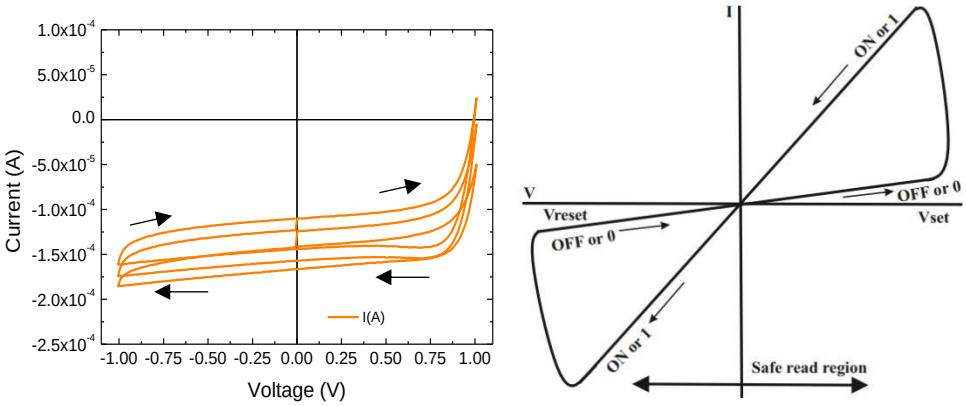

Figure A2.: Left) Bottle-shaped curve, Right) Crossed loop curve.

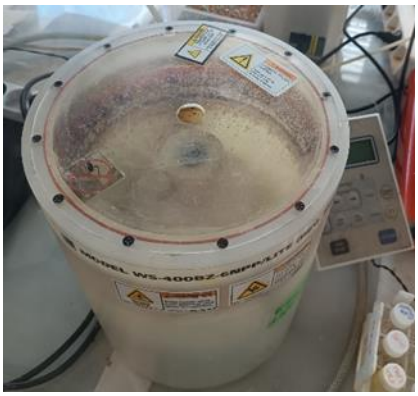

Figure A3.: WS-400BZ-&NPP/LITE spin-coater device.

Figure A4.: UV Ozone CleanerTM by Bioforce Nanosciences

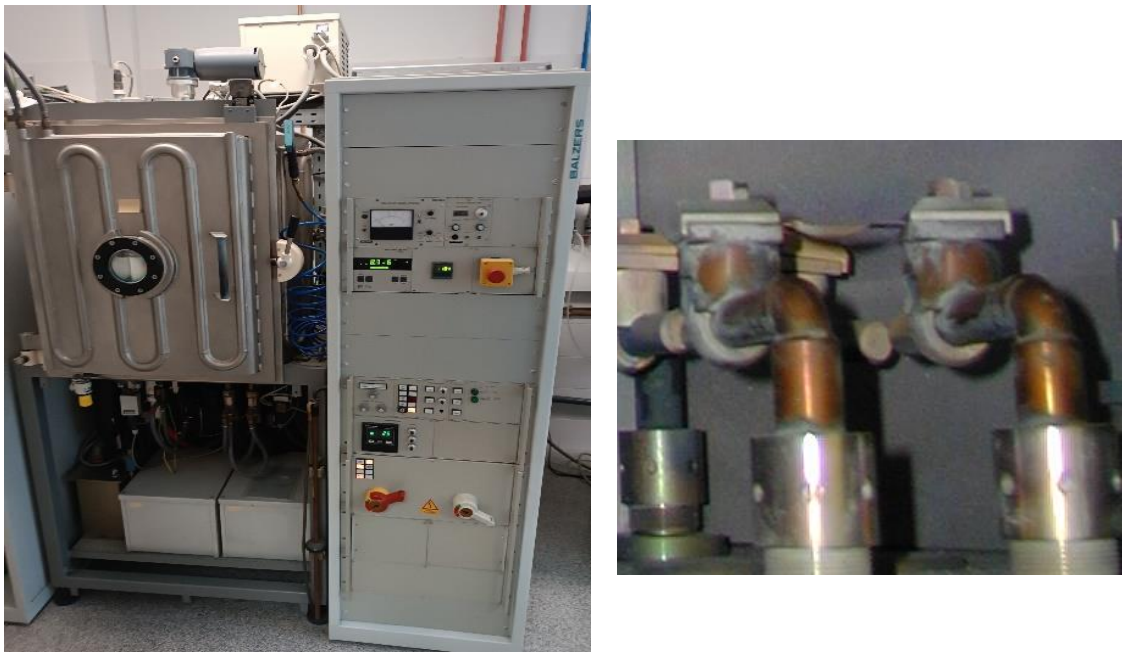

Figure A5.: Left) Thermal evaporator used for gold electrode deposition. Right) Thermal evaporator metallic boat which generates evaporated gold.

Figure A6.: Autolab PGSTAT101

Table A1: PV and memristor parameters of sample 1-4 .

Structure		Solar Cell						Memristor			
	NR.	Scan direction	PCE (%)	J_{sc} (mA/cm^2)	V_{oc} (V)	FF (%)	HI	ON/OFF ratio	V_{set}	V_{reset}	Endurance time (40 cycles)
	**1**	REV	8.3	14.04	1.01	59	0.63	2.59	-0.63	-0.30	NO
		FWD	3.1	12.91	0.84	32					
	2	REV	6.9	13.08	0.98	54	0.54	3.49	-0.70	-0.27	NO
		FWD	3.2	11.43	0.91	31				-	
	3	REV	5.5	11.69	0.95	49	0.44	2.63	-0.70	-0.23	NO
		FWD	3.1	10.09	0.88	36				-	
	4	REV	4.1	9.76	0.90	47	0.56	3.80	-0.78	-0.25	NO
		FWD	1.8	6.87	0.71	36					

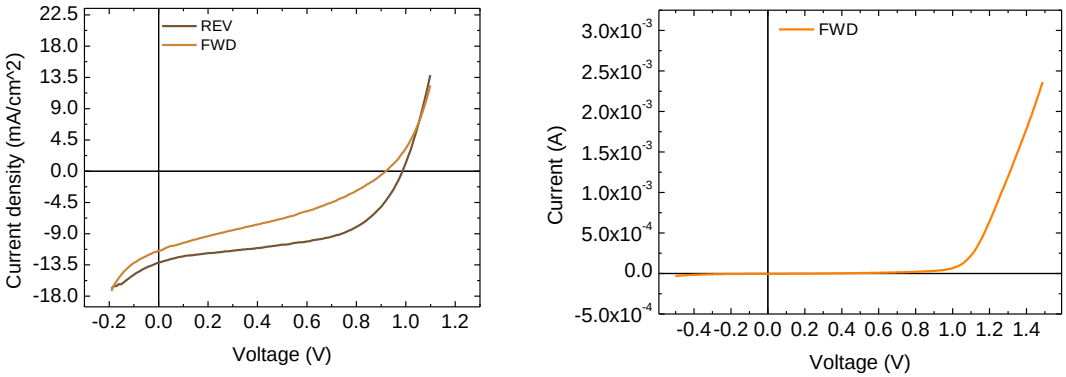

Figure A7.: **Sample 2:** Left) J-V curve under 1 sun illumination

Right) I-V curve dark conditions

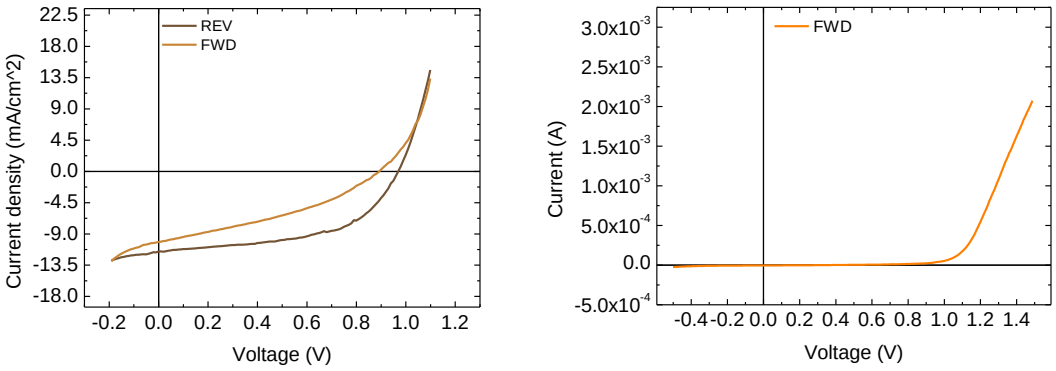

Figure A8.: **Sample 3:** Left) J-V curve under 1 sun illumination

Right) I-V curve dark conditions.

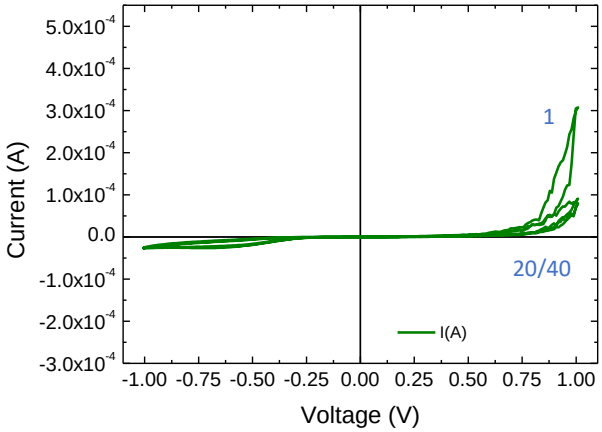

Figure A9.: Cyclic voltammetry of **sample 1** in dark conditions

(Only cycle 1st, 20th and 40th are represented.)

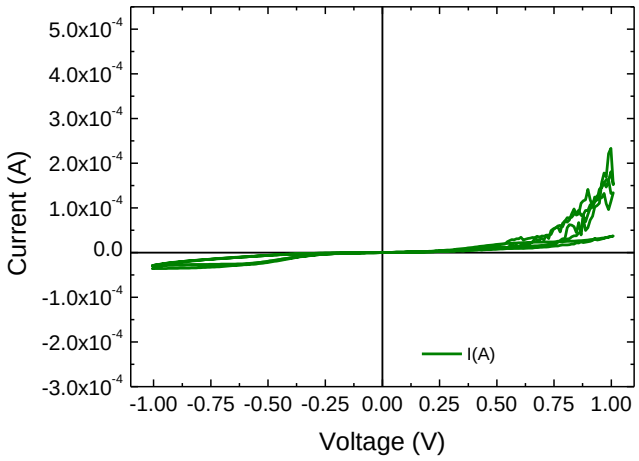

Figure A10.: Cyclic voltammetry of **sample 2** in dark conditions.

(Only cycle 1st, 20th and 40th are represented.)

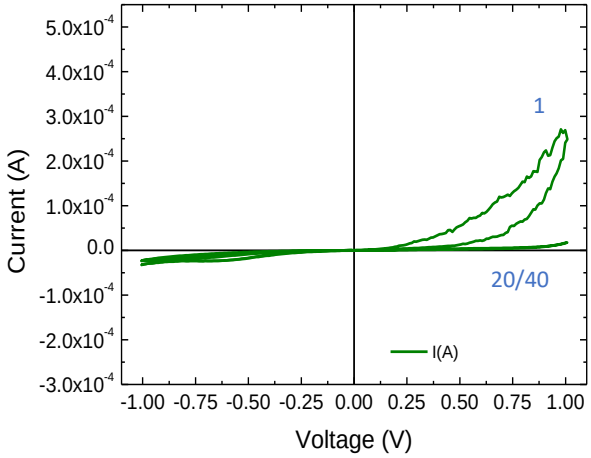

Figure A11.: Cyclic voltammetry of **sample 3** in dark conditions.

(Only cycle 1st, 20th and 40th are represented.)

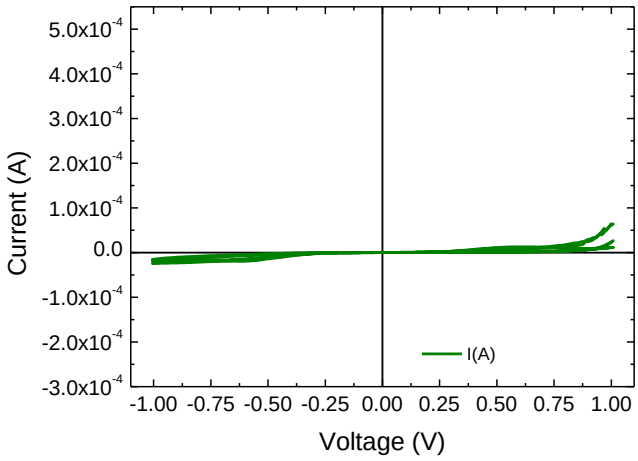

Figure A12.: Cyclic voltammetry of **sample 4** in dark conditions.

(Only cycle 1st, 20th and 40th are represented.)

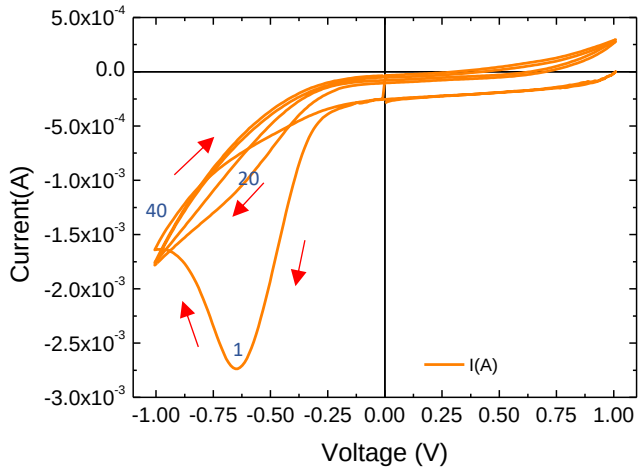

Figure A13.: Cyclic voltammetry of **sample 2** under 1 sun illumination.

(Only cycle 1st, 20th and 40th are represented.)

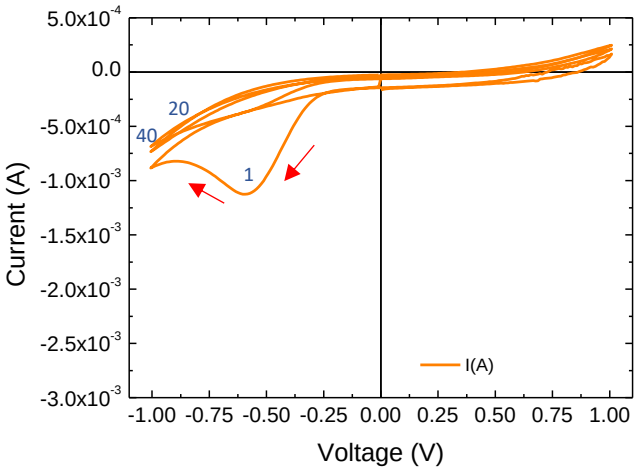

Figure A14.: Cyclic voltammetry of **sample 3** under 1 sun illumination.

(Only cycle 1st, 20th and 40th are represented.)

Table A2.: PV and memristor parameters of sample 5-8.

Structure		Solar Cell						Memristor			
	N R.	Scan direction	PCE (%)	J_{sc} (mA/ cm^2)	V_{oc} (V)	FF (%)	HI	ON/OFF ratio	V_{set}	V_{reset}	Endurance time (40 cycles)
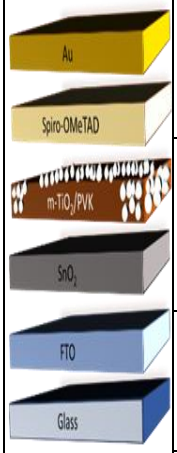	**5**	REV	9.4	15.13	0.95	66	0.43	1.15	-	-0.29	YES
		FWD	5.4	12.75	0.97	43				-0.80	
	6	REV	7.3	11.73	0.97	64	0.51	1.34	-	-0.28	YES
		FWD	3.6	9.15	0.97	40				-0.84	
	7	REV	2.5	9.58	0.70	37	0.64	-	-	-	-
		FWD	0.9	7.78	0.43	28					
	8	REV	2.1	10.94	0.63	31	0.71	-	-	-	-
		FWD	0.6	8.66	0.28	26					

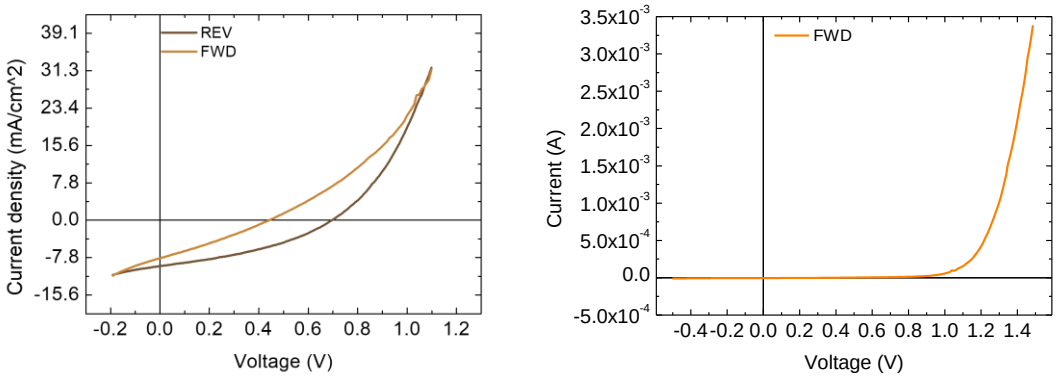

Figure A15.: Sample 7: Left) J-V curve under 1 sun illumination.

Right) I-V curve dark conditions

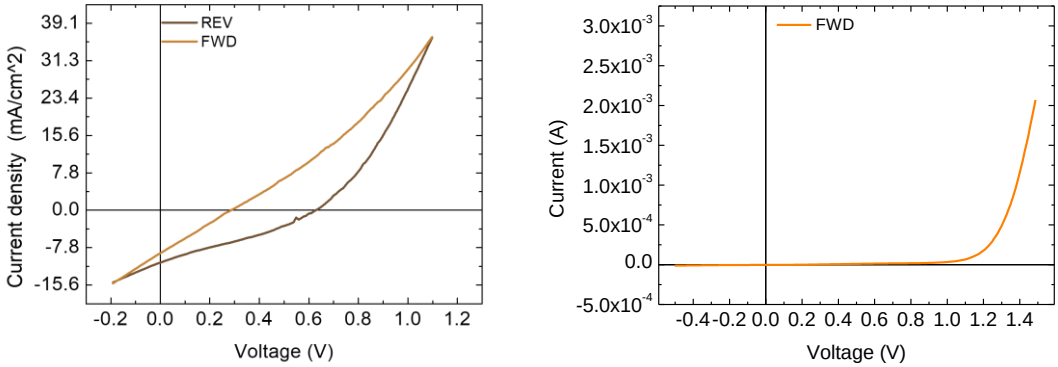

Figure A16.: **Sample 8:** Left) J-V curve under 1 sun illumination.

Right) I-V curve dark conditions

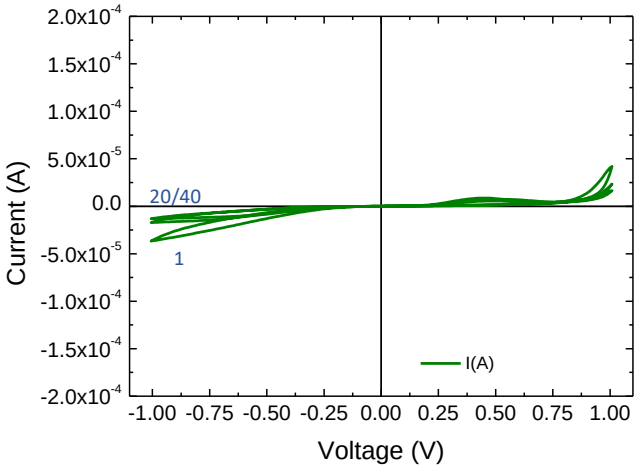

Figure A17.: Cyclic voltammetry of **sample 6** in dark conditions.

(Only cycle 1st, 20th and 40th are represented.)

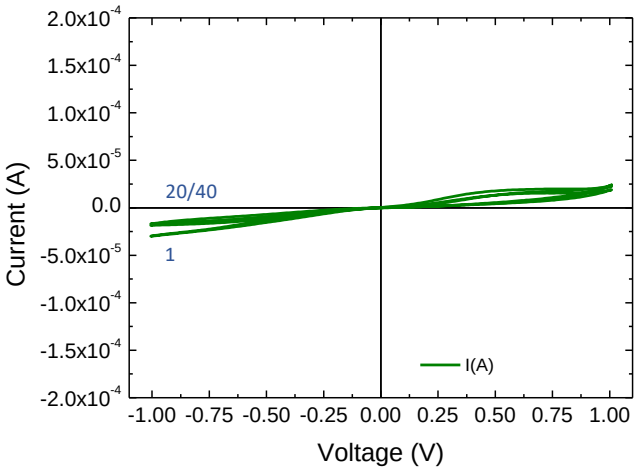

Figure A18.: Cyclic voltammetry of **sample 7** in dark conditions.

(Only cycle 1st, 20th and 40th are represented.)

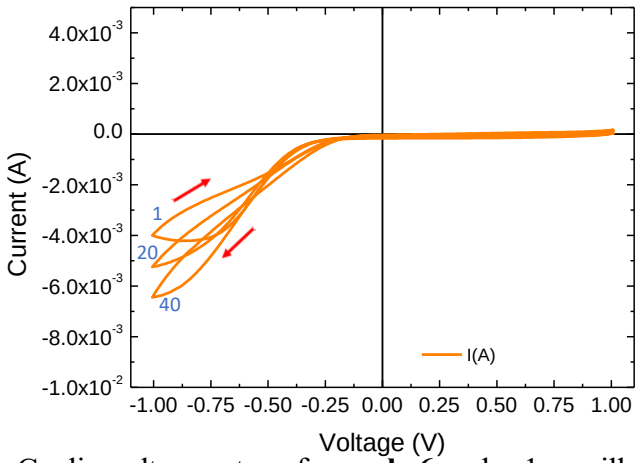

Figure A19.: Cyclic voltammetry of **sample 6** under 1 sun illumination.

(Only cycle 1st, 20th and 40th are represented.)

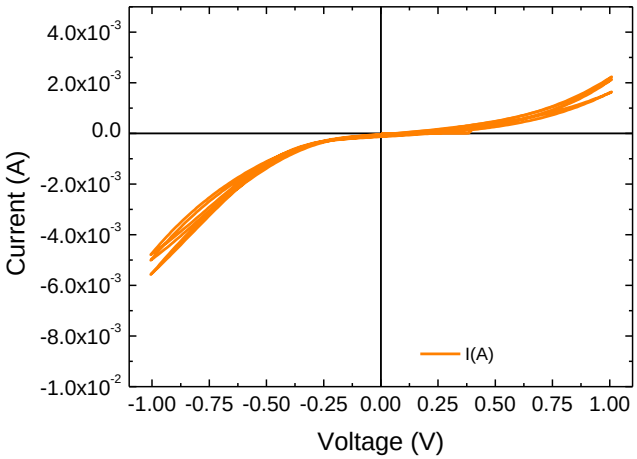

Figure A20.: Cyclic voltammetry of **sample 7** under 1 sun illumination.

(Only cycle 1st, 20th and 40th are represented.)

Table A3.: PV and memristor parameters of sampleS 9-12.

Structure		Solar Cell						Memristor			
	Sample NR.	Scan direction	PCE (%)	J_{sc} (mA/cm^2)	V_{oc} (V)	FF (%)	Hysteresis index	ON /OFF ratio	V_{set}	V_{reset}	Endurance time (40 cycles)
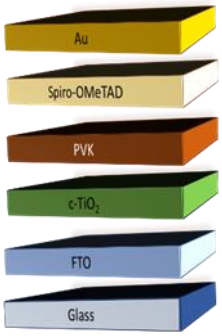	**9**	REV	8.9	-12.46	1.03	68	0.36	1.45	0.79	-	YES (Increase with cycles)
		FWD	5.7	-10.32	1.01	54					
	10	REV	7.3	-9.20	1.04	64	0.37	1.52	0.80	-	YES (Increase with cycles)
		FWD	4.6	-7.70	1.05	51					
	11	REV 3	5.4	-11.41	0.93	56	0.48	-	-	-	-
		FWD	2.8	-8.55	0.73	45					
	12	REV	5.2	-7.14	1.02	62	0.38	1.29	0.75	-	YES (Increase with cycles)
		RWD	4.5	-6.09	1.02	56					

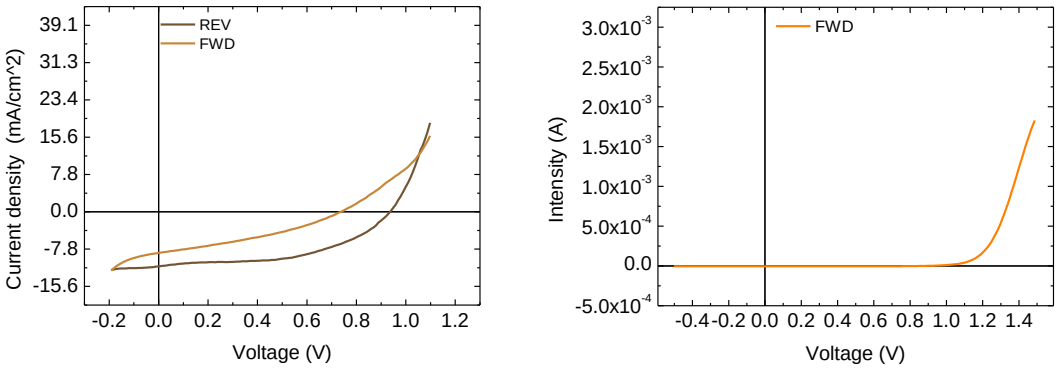

Figure A21.: **Sample 11:** Left) J-V curve under 1 sun illumination

Right) I-V curve dark conditions

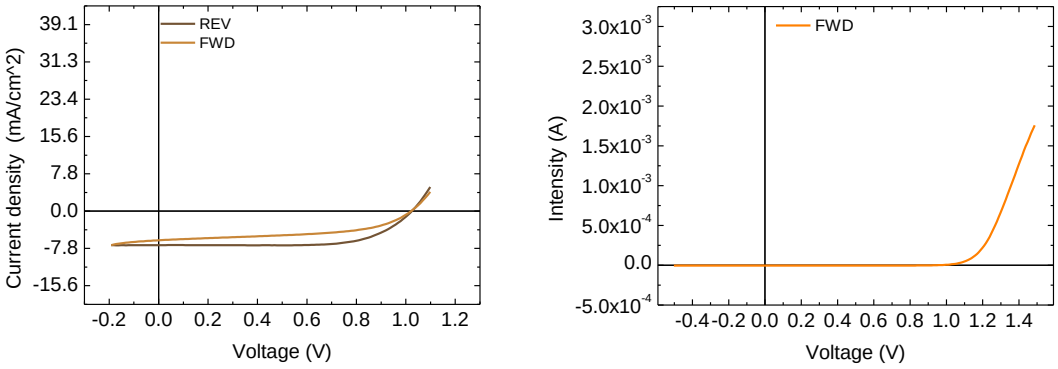

Figure A22.: **Sample 12:** Left) J-V curve under 1 sun illumination.

Right) I-V curve dark conditions

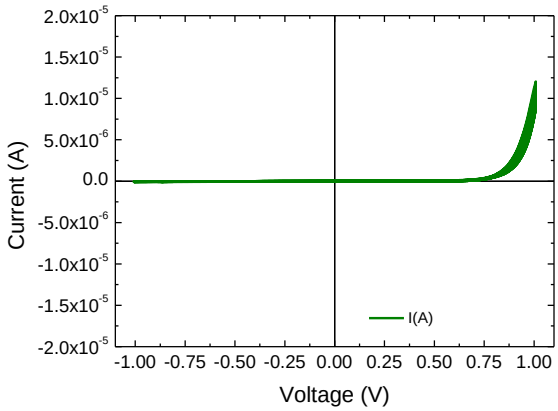

Figure A23.: Cyclic voltammetry of **sample 11** in dark conditions.

(Only cycle 1st, 20th and 40th are represented.)

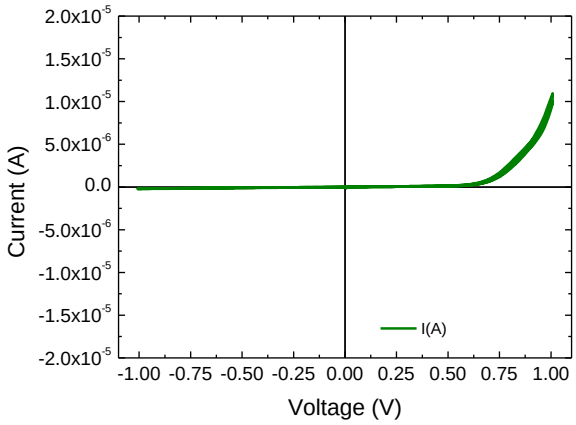

Figure A24.: Cyclic voltammetry of **sample 12** in dark conditions.

(Only cycle 1st, 20th and 40th are represented.)

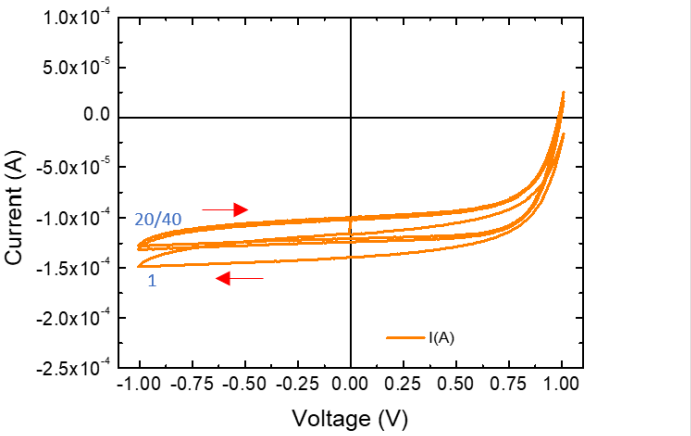

Figure A25.: Cyclic voltammetry of **sample 12** under 1 sun illumination.

(Only cycle 1st, 20th and 40th are represented.)

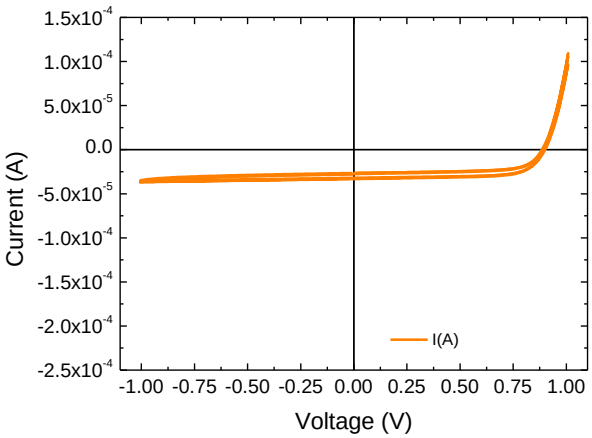

Figure A26.: Cyclic voltammetry of sample **11** under 1 sun illumination.

(Only cycle 1st, 20th and 40th are represented.)

Table A4.: PV and memristor parameters of sample 13-16.

Structure		Solar Cell						Memristor			
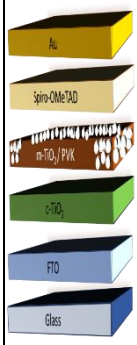	NR.	Scan direction	PCE (%)	J_{sc} (mA/cm^2)	V_{oc} (V)	FF (%)	HI	ON/OFF ratio	V_{set}	V_{reset}	Endurance time (40 cycles)
	13	REV	4.7	-7.49	0.98	64	0.49	3.07	0.68	-	YES
		FWD	2.4	-6.08	0.97	41					
	14	REV	4.3	-12.42	0.96	57	0.51	3.70	0.78	-	YES
		FWD	2.1	-10.82	0.9	31					
	15	REV	2.9	-5.01	0.99	63	0.24	1.48	0.71	-	YES
		FWD	2.2	-3.81	0.99	46					
	16	REV	2.5	-15.94	0.91	47	0.2	2.24	0.69	-	YES

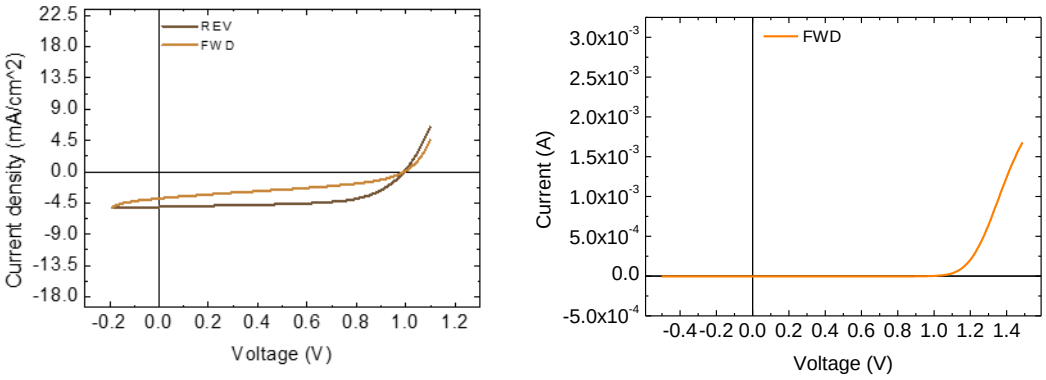

Figure A27.: Sample 15: Left) J-V curve under 1 sun illumination Right) I-V curve dark conditions

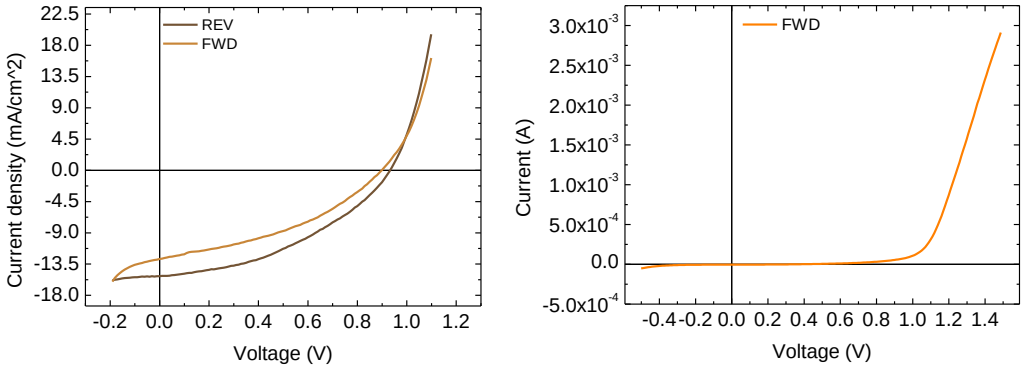

Figure A28.: Sample 16: Left) J-V curve under 1 sun illumination Right)I-V curve dark conditions

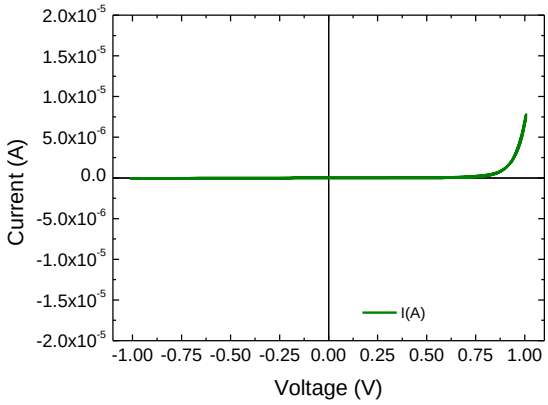

Figure A29.: Cyclic voltammetry of **sample 15** in dark conditions. (Only cycle 1st, 20th and 40th are represented.)

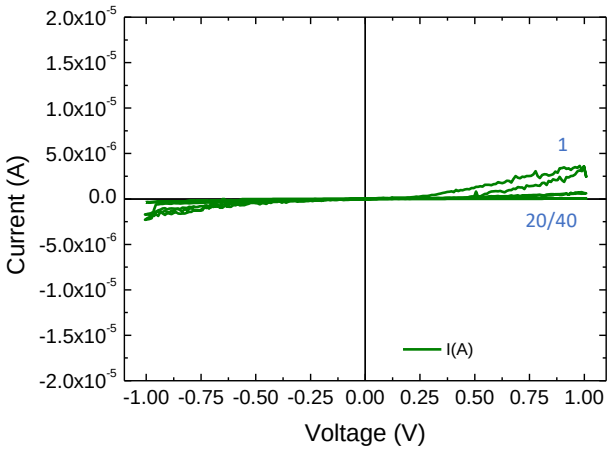

Figure A30.: Cyclic voltammetry of **sample 16** in dark conditions.
(Only cycle 1st, 20th and 40th are represented.)

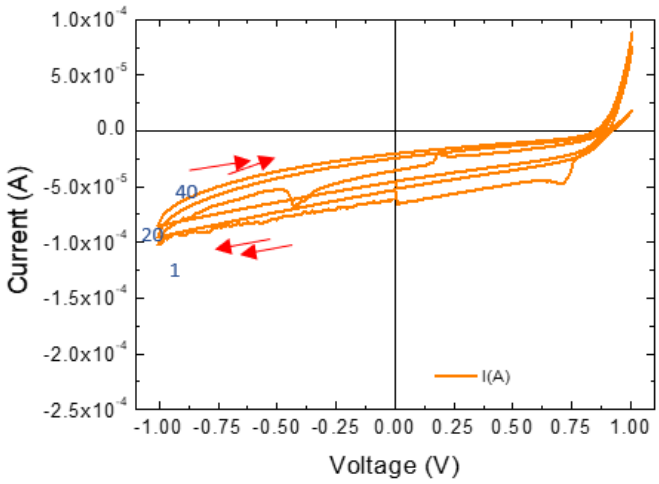

Figure A31.: Cyclic voltammetry of **sample 15** under 1 sun illumination.
(Only cycle 1st, 20th and 40th are represented.)

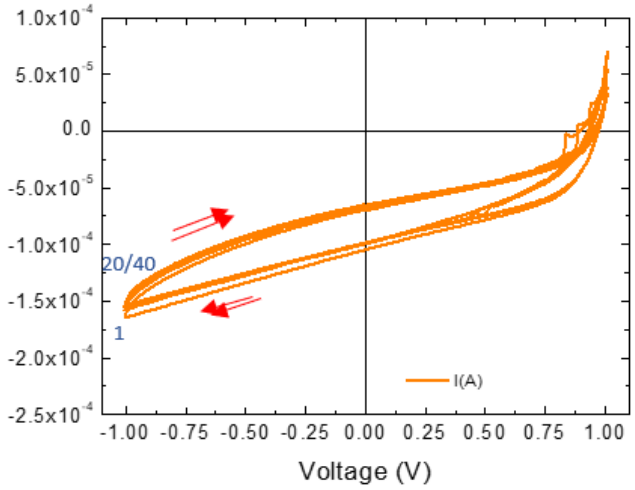

Figure A32.: Cyclic voltammetry of **sample 16** under 1 sun illumination. (Only cycle 1st, 20th and 40th are represented.)

Table A5: Main average values of all structures studied

Device layout	PCE(%)	HI	ON/OFF RATIO	V_{set} (V)	V_{reset} (V)	Endurance 40 cycles
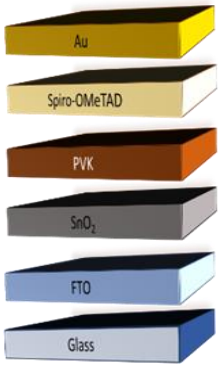	6.2 ±1.8	0.63± 0.07	3.13 ± 0.61	-0.26 ± 0.06	-0.70 ± 0.03	NO
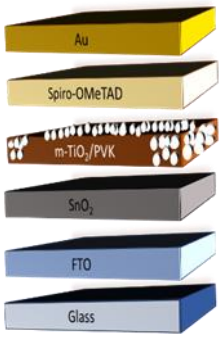	5.3 ±3.6	0.57± 0.13	1.25 ± 0.13	-0.29 ± 0.01	-0.82 ± 0.03	YES
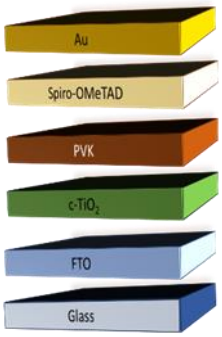	6.7 ± 1.8	0.40± 0.06	1.42 ± 0.12	0.79 ± 0.03	-	YES (Increase with cycles)
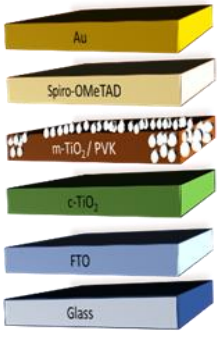	3.6 ± 1.0	0.36 ± 0.16	2.62 ± 0.97	0.72 ± 0.05	-	YES

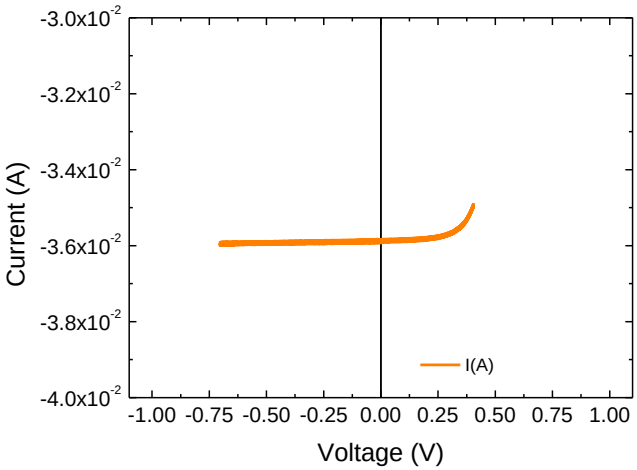

Figure A33.: Cyclic Voltammetry of 'Silicon PV' under 1 sun illumination. (Only cycle 1st, 20th and 40th are represented.)

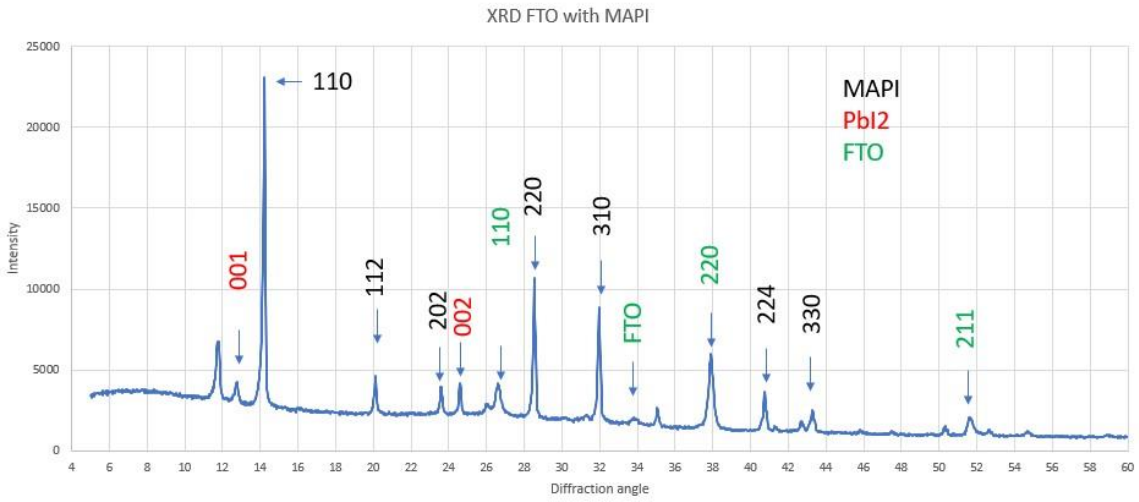

Figure A34.: XRD analysis of FTO-MAPIperovskite.